VDA | Verband der Automobilindustrie

FAT | Forschungsvereinigung Automobiltechnik

# FAT-Schriftenreihe 361

## Compatibility of polymers for fuel cell automobiles

# Compatibility of polymers for fuel cell automobiles

**Forschungsstelle**

Max-Planck-Insitut für Polymerforschung

Prof. Katharina Landfester / Dr. Svenja Morsbach / Dr. Kai Zhang

Das Forschungsprojekt wurde mit Mitteln der Forschungsvereinigung Automobiltechnik e.V. (FAT) gefördert.

MAX PLANCK INSTITUTE
FOR POLYMER RESEARCH

# Final report for the research cooperation FAT – MPIP „Compatibility of polymers for fuel cell automobiles"

**Prof. Katharina Landfester / Dr. Svenja Morsbach / Dr. Kai Zhang**

## Content:

## 1. General objectives

The general aim of the project was to identify suitable methods for the characterization of polymer materials in fuel cell automobiles. Within the current architecture of fuel cell automobiles, polymers are applied in various places such as seals in the form of O-rings or polymer liners. Upon sustained contact with hydrogen, different aging processes can occur, which potentially lead to hydrogen leakage and, thus, pose significant security risks. Therefore, it is of utmost importance to develop a set of obligatory specifications for the used materials, potentially resulting in standardization guidelines or legal regulations for the automobile industry.

In this context, different physical and chemical analysis methods should be utilized to allow for a pre-screening of polymers after accelerated aging conditions in contact with hydrogen. Ultimately, they should give information about possible tests for standardization and regulatory aspects.

The applied characterization methods (as well as potential method developments/advancements) should be evaluated concerning the following factors:

- operation effort

- reproducibility

- resources

- significance and robustness

In a first step, suitable polymer material samples should be defined (covering a range of different materials and sample shapes/species). Secondly, treatment conditions for an accelerated aging process in hydrogen atmosphere should be set up. This should include the characterization of the initial thermal stability of samples to ensure that the materials are not compromised due to elevated temperatures. Subsequently, all samples should undergo hydrogen aging treatment. All samples are analyzed before and after the treatment and all possible changes are evaluated.

The work presented in this report is in part already published in the journal *Energy Technology* (2022), 2200018, DOI: 10.1002/ente.202200018 (CC BY 4.0).

# 2. Sample Overview

## 2.1 Identified Materials

Within the project group, several typical polymer materials were identified. These materials include 1) thermoplastic polyurethane (TPU), 2) polyether ether ketone (PEEK), 3) polyurethane (PU), and 4) fluoroelastomer (FKM). Additionally, two different sample species were selected: shouldered test bars/flat cut specimen and O-rings. The following list includes the overview about all characterized samples:

**Table 2.1.** List of samples and materials included in the project

| Sample ID | Sample description |
|---|---|
| FAT_001 | TPU – shouldered test bars + flat cut specimen |
| FAT_002 | PEEK – shouldered test bars |
| FAT_003 | PU – O-rings (blue) |
| FAT_004 | PU – O-rings (turquoise) |
| FAT_005 | FKM – O-rings |

## 2.2 Treatment conditions

Treatment with hydrogen should be done under increased pressure and elevated temperature conditions to accelerate the potential aging process and make changes detectable within experimentally reasonable timeframes. Thus, all samples were subjected to thermogravimetric analysis prior to the aging treatment to determine their respective decomposition temperatures (detailed results see section 3.3) in $N_2$ or synthetic air atmosphere. For all samples, it was found that decomposition only occurred above a temperature of 200 °C or higher. Accordingly, the parameters for incubation in hydrogen were fixed as follows:

$T$ = 80 °C, $p$ = 85 bar, $t$ = 335 hours

# 3. Results and Discussion

All samples were subjected to several characterization techniques before and after $H_2$ incubation treatment. To evaluate different aspects of possible changes, the sample morphology, molecular weight, thermal properties, rheological behavior, $H_2$ absorption and chemical composition were determined.

## 3.1 Morphological characterization

For morphological characterization of the samples before and after hydrogen incubation, scanning electron microscopy (SEM) imaging was conducted on all samples in two different ways. First the surface of each sample (i.e. the hydrogen contact area) was imaged at different magnifications. Second, the freeze fracture surface of all samples was inspected by SEM. For this, samples were cooled in liquid nitrogen and subsequently mechanically broken. The fracture surface was imaged at different magnifications.

Figure 3.1 shows the sample surface of FAT_001 (TPU) before and after hydrogen incubation. Before hydrogen treatment the surface was relatively smooth with minor roughness in the lower micrometer range. After hydrogen incubation, the roughness of the surface increased significantly, indicating a substantial reaction to the incubation conditions. In principle, this could either be a result of material compression due to the high pressure or material that was 'washed out' from in between the micrometer sized particles. However, it seems unlikely that under hydrogen atmosphere PU material would be washed out. Rather, this could potentially be attributed to the different hardness of the PU segments, meaning that softer segments in the material might be compressed to a higher degree than the hard segments. In this case, the recorded effect might not be specific to hydrogen incubation but also occur in other atmospheres. For future investigations, a control/reference experiment should be performed by e.g. comparing to incubation in nitrogen atmosphere under the same conditions.

In figure 3.2, images of the freeze fracture surfaces of the same samples are shown. Both, before and after the hydrogen incubation, small pores are visible throughout the material, which might be result of the manufacturing process. The general appearance of the material did not change after hydrogen treatment, indicating an overall effect only on the sample surface.

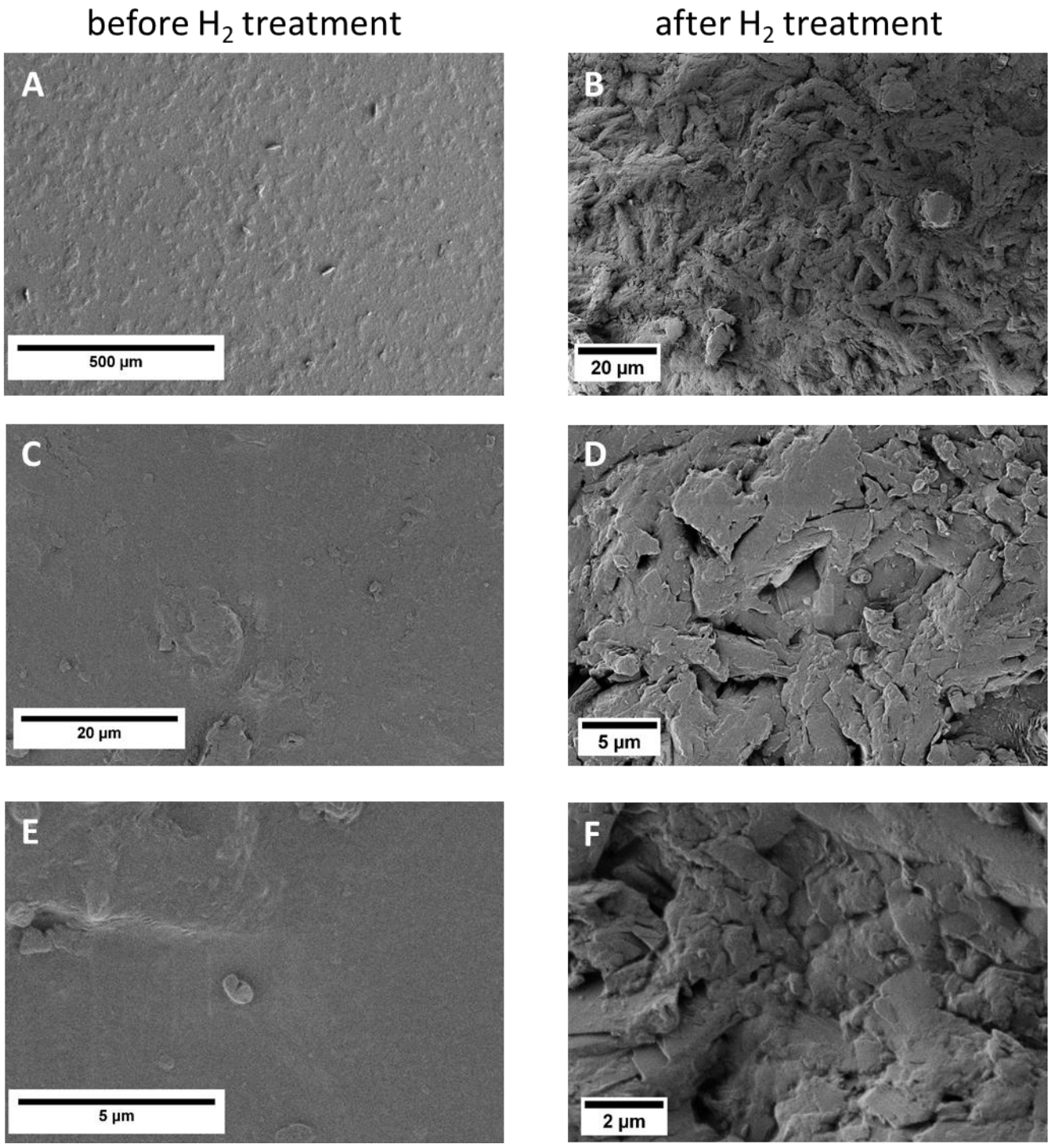


**Figure 3.1.** Scanning electron microscopy (SEM) images of the sample surface of FAT_001 (TPU) before (A, C, E) and after hydrogen incubation (B, D, F) shown at different magnifications.[1]

[1] Figure modified from Morsbach et al., Hydrogen Compatibility of Polymers for Fuel Cell Vehicles, Energy Technology 2022, 2200018, DOI: 10.1002/ente.202200018 (CC BY 4.0).

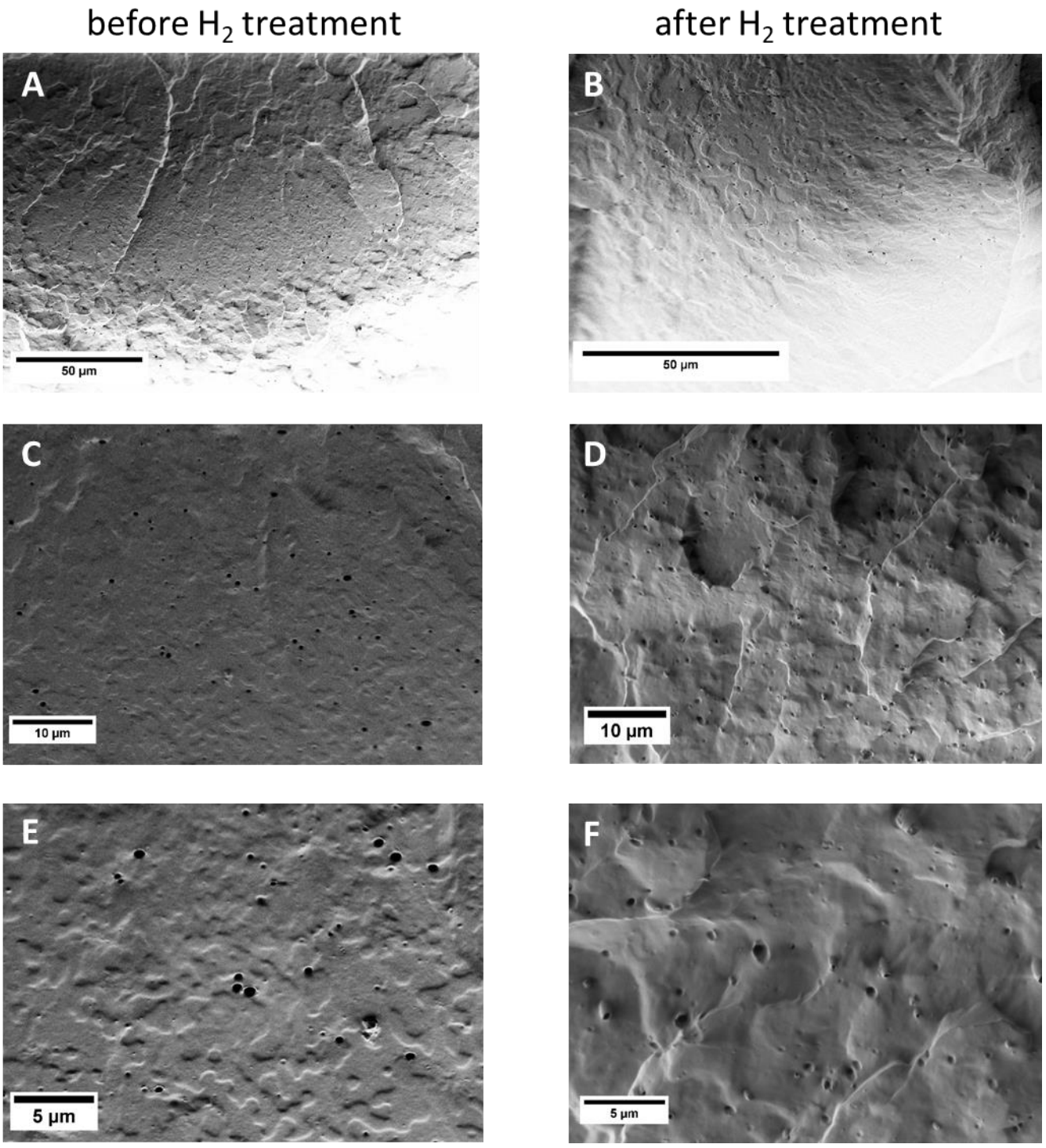


**Figure 3.2.** Scanning electron microscopy (SEM) images of the freeze fracture surface of sample FAT_001 (TPU) before (A, C, E) and after hydrogen incubation (B, D, F) shown at different magnifications.

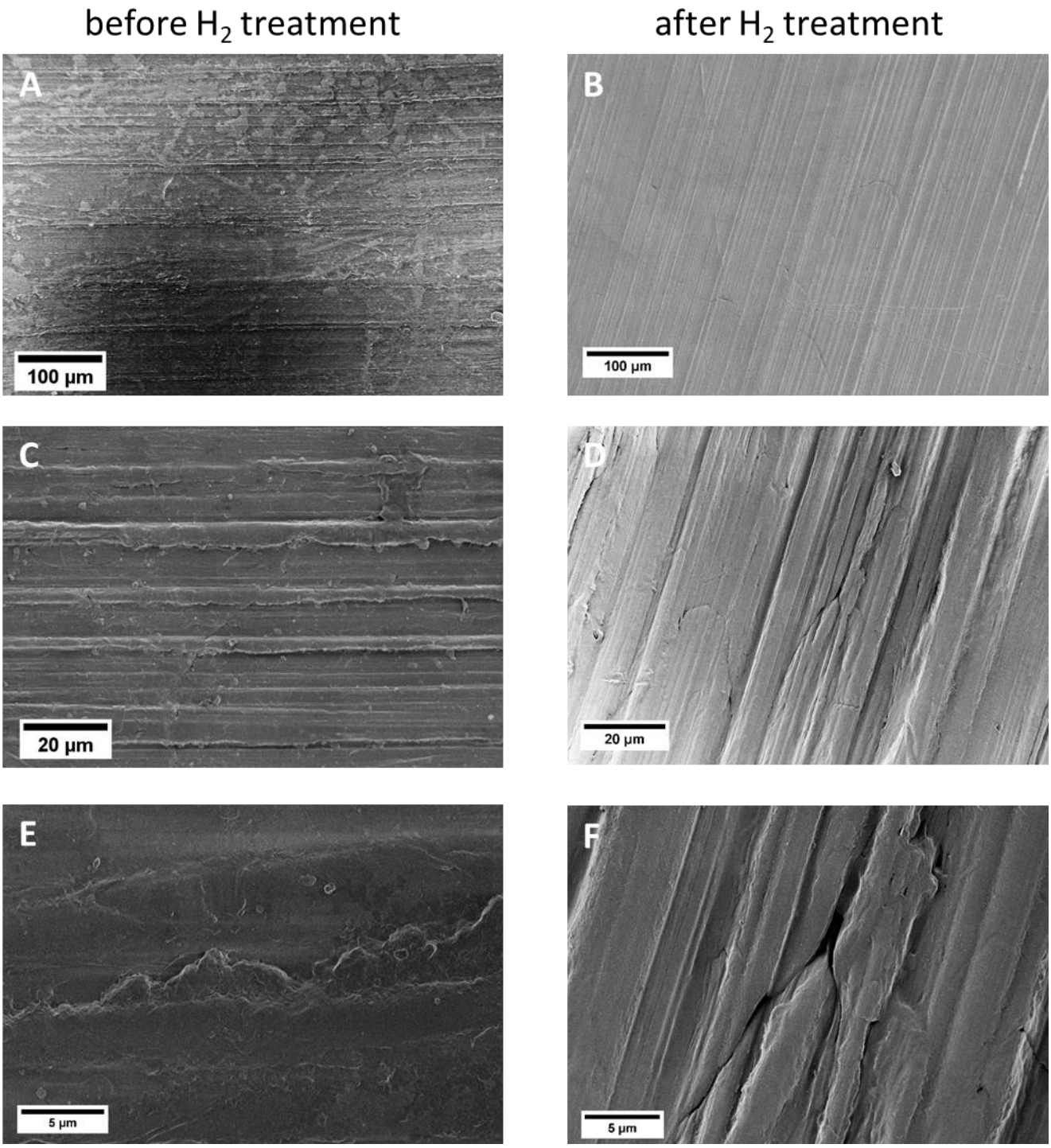


**Figure 3.3.** Scanning electron microscopy (SEM) images of the sample surface of FAT_002 (PEEK) before (A, C, E) and after hydrogen incubation (B, D, F) shown at different magnifications.[2]

[2] Figure modified from Morsbach et al., Hydrogen Compatibility of Polymers for Fuel Cell Vehicles, Energy Technology 2022, 2200018, DOI: 10.1002/ente.202200018 (CC BY 4.0).

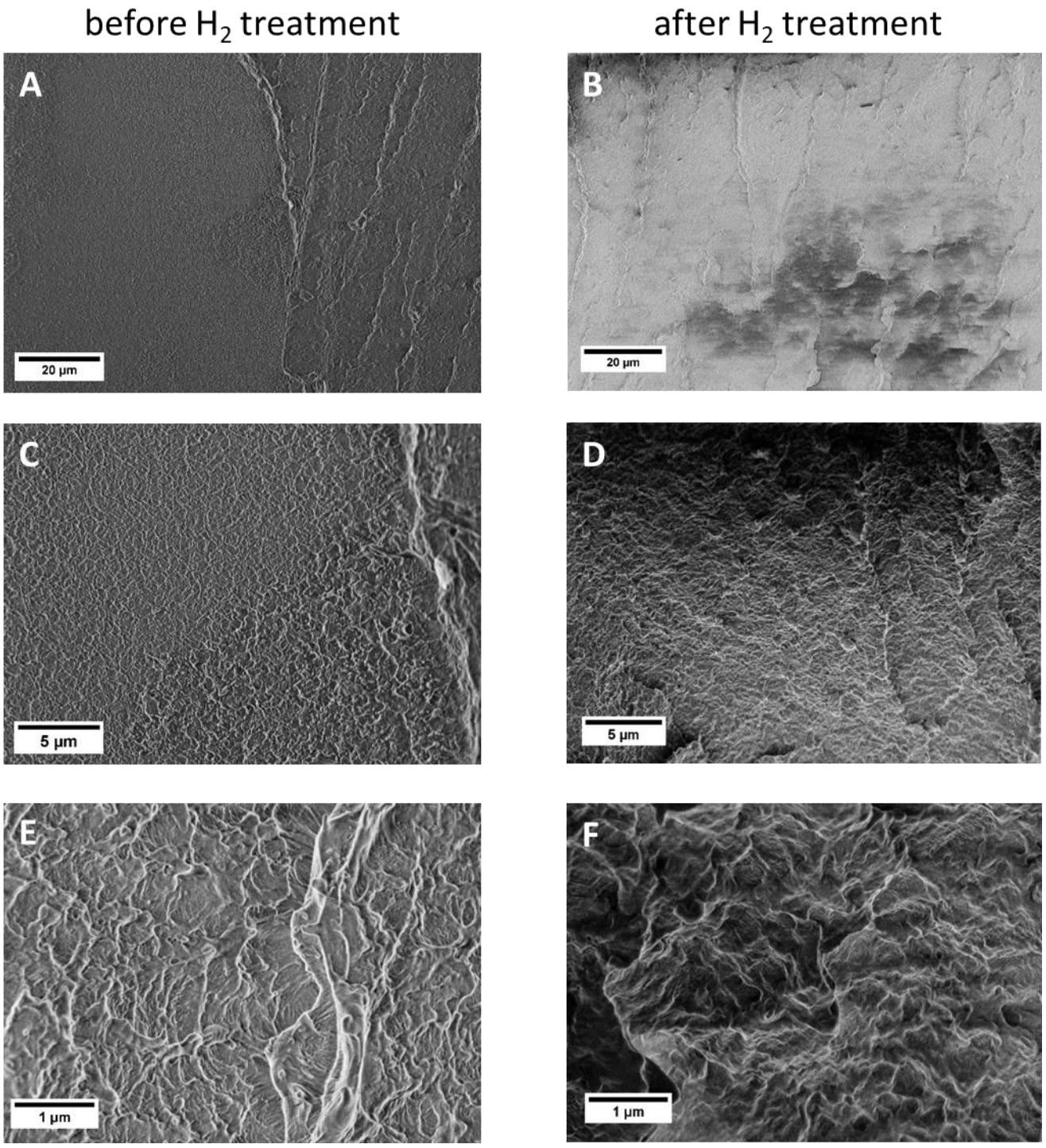


**Figure 3.4.** Scanning electron microscopy (SEM) images of the freeze fracture surface of sample FAT_002 (PEEK) before (A, C, E) and after hydrogen incubation (B, D, F) shown at different magnifications.

Figure 3.3 shows images of the sample surface of FAT_002 (PEEK) before and after hydrogen incubation. In both cases, irregular creasing can be detected probably stemming from the sample manufacturing process. After the hydrogen treatment, in some areas cracks were found on the surface. In all cases, the edges of the cracks were rather smooth. This might suggest, that the cracks were already present in the material before the hydrogen incubation. However, this is not completely clear, since the imaging was performed on two different sample specimen. For future investigations, we suggest to image the same sample specimen before and after the hydrogen treatment.

In figure 3.4, freeze fracture surfaces of the same sample FAT_002 are shown before and after hydrogen incubation. The material shows a roughness on the nanometer scale, but no significant differences can be found in the two sample types. This also suggests that any changes potentially resulting from hydrogen contact might only concern the sample surface.

Figure 3.5 shows the sample surface of FAT_003 (PU) before and after hydrogen incubation. The sample surface in both cases contains regular indentations (spacing of roughly 150 µm) from the manufacturing of the O-ring. Apart from this, the material surface appeared very smooth and did not change before and after the hydrogen treatment.

In contrast, in figure 3.6 the freeze fracture surface of the material shown present a different result. Before hydrogen incubation, seemingly crystalline domains spanning several tens of micrometers could be found throughout the material with small nanometer sized particles probably acting as seed crystals. After hydrogen incubation, these crystalline domains cannot be distinguished anymore. However, the small particles were still visible. This suggests that a physical rearrangement of the polymer might have occurred throughout the whole material, while the surface roughness of the sample was unaffected.

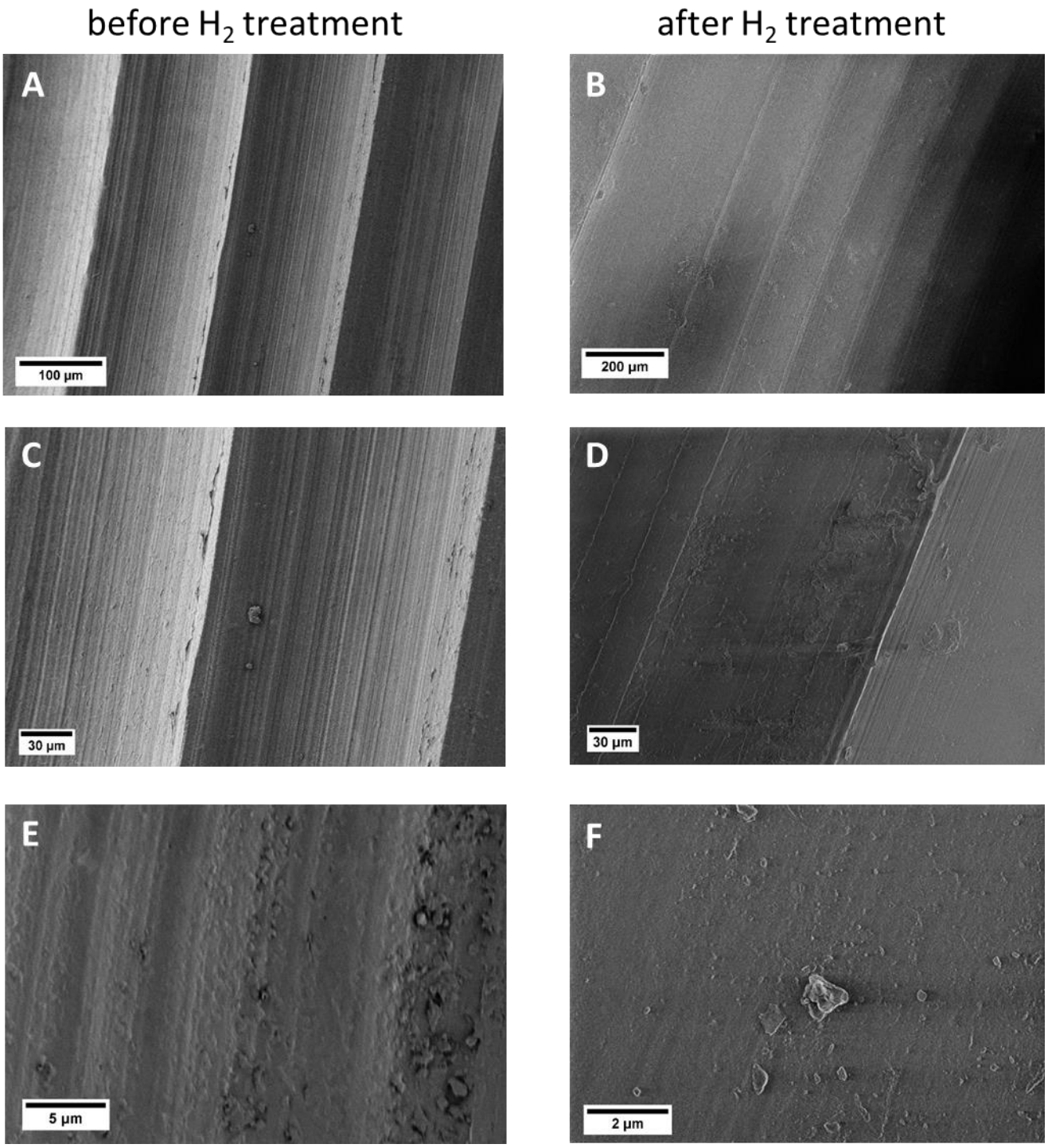


**Figure 3.5.** Scanning electron microscopy (SEM) images of the sample surface of FAT_003 (PU) before (A, C, E) and after hydrogen incubation (B, D, F) shown at different magnifications.

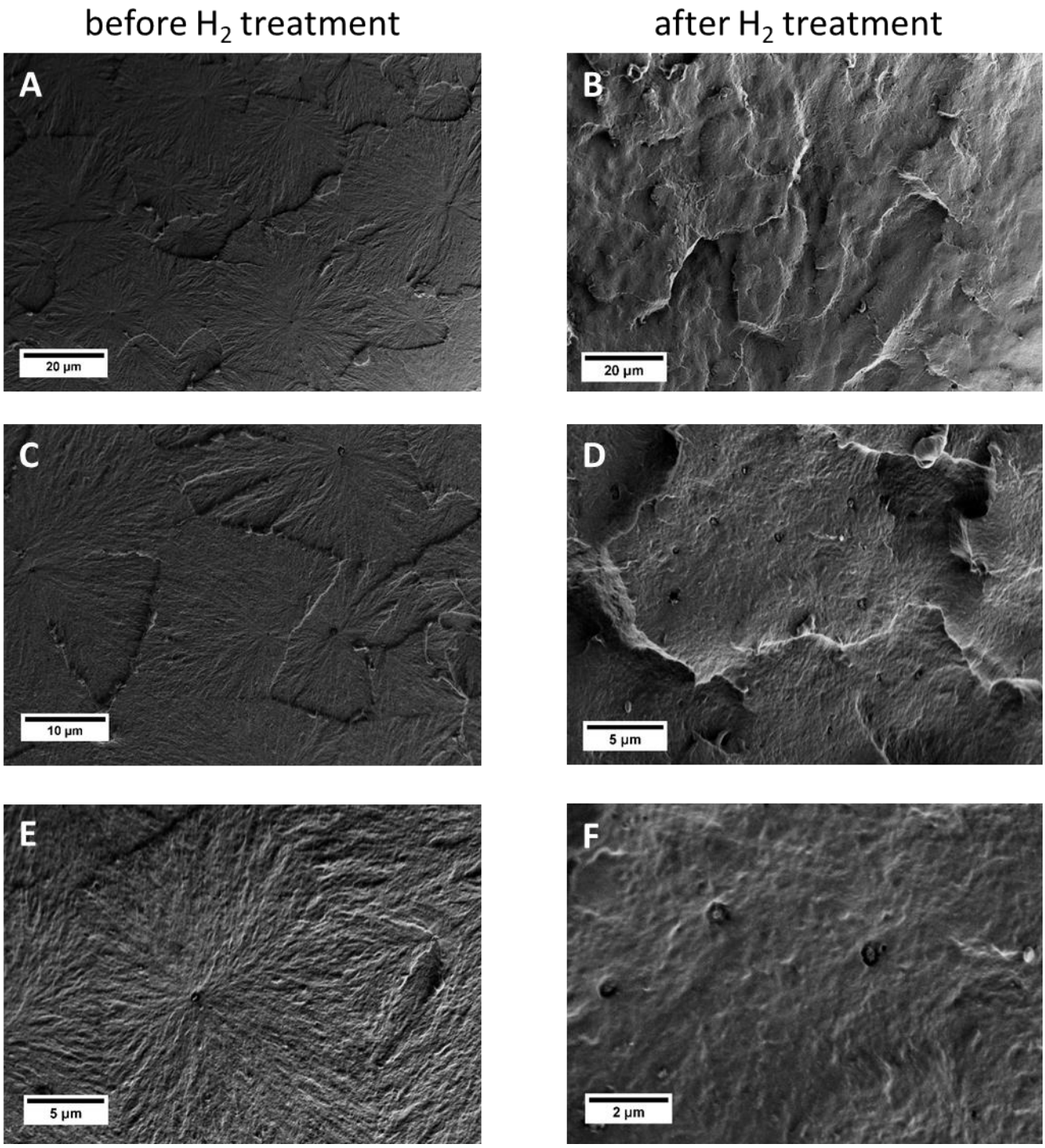


**Figure 3.6.** Scanning electron microscopy (SEM) images of the freeze fracture surface of sample FAT_003 (PU) before (A, C, E) and after hydrogen incubation (B, D, F) shown at different magnifications.[3]

[3] Figure modified from Morsbach et al., Hydrogen Compatibility of Polymers for Fuel Cell Vehicles, Energy Technology 2022, 2200018, DOI: 10.1002/ente.202200018 (CC BY 4.0).

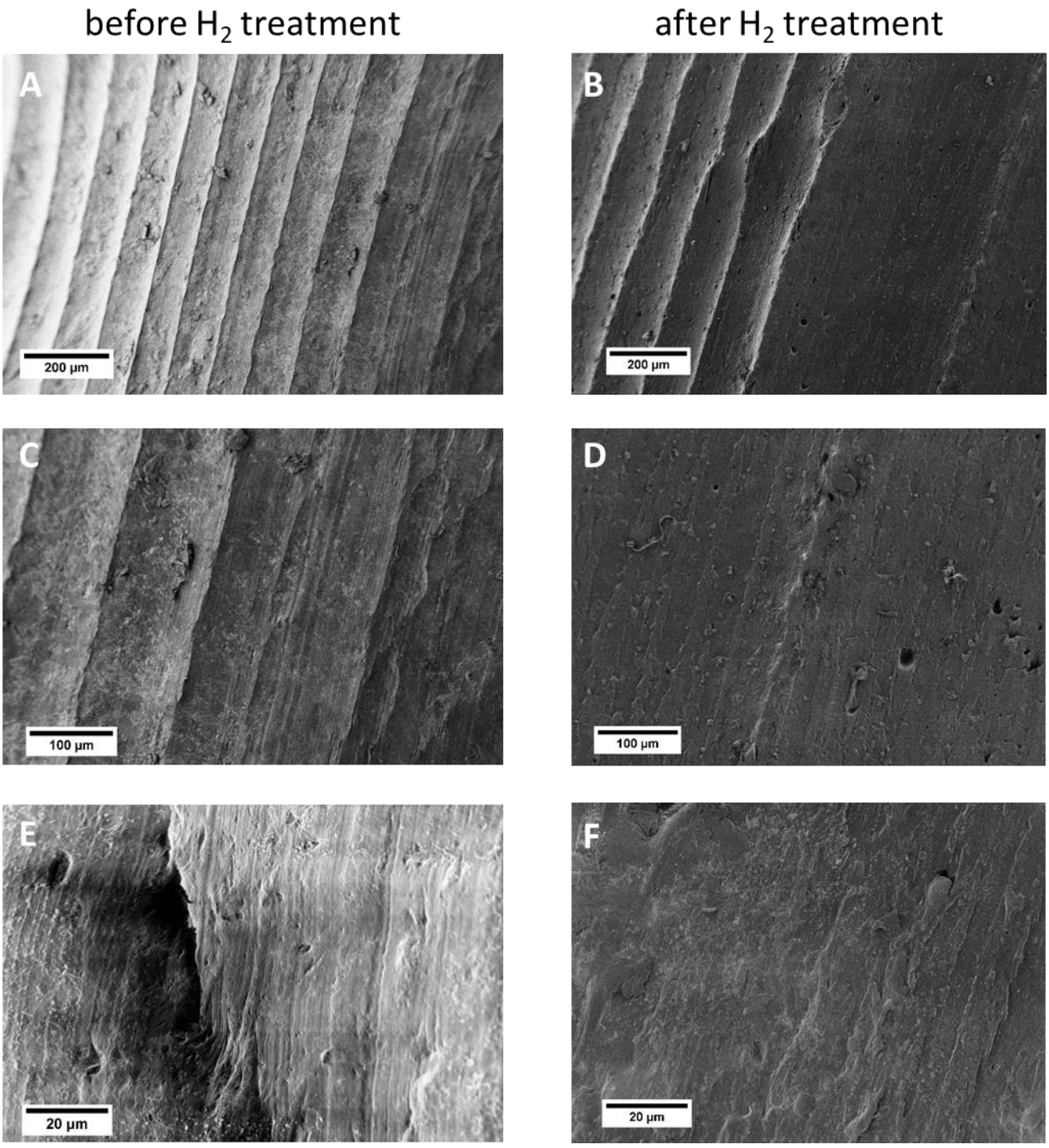


**Figure 3.7.** Scanning electron microscopy (SEM) images of the sample surface of FAT_004 (PU) before (A, C, E) and after hydrogen incubation (B, D, F) shown at different magnifications.

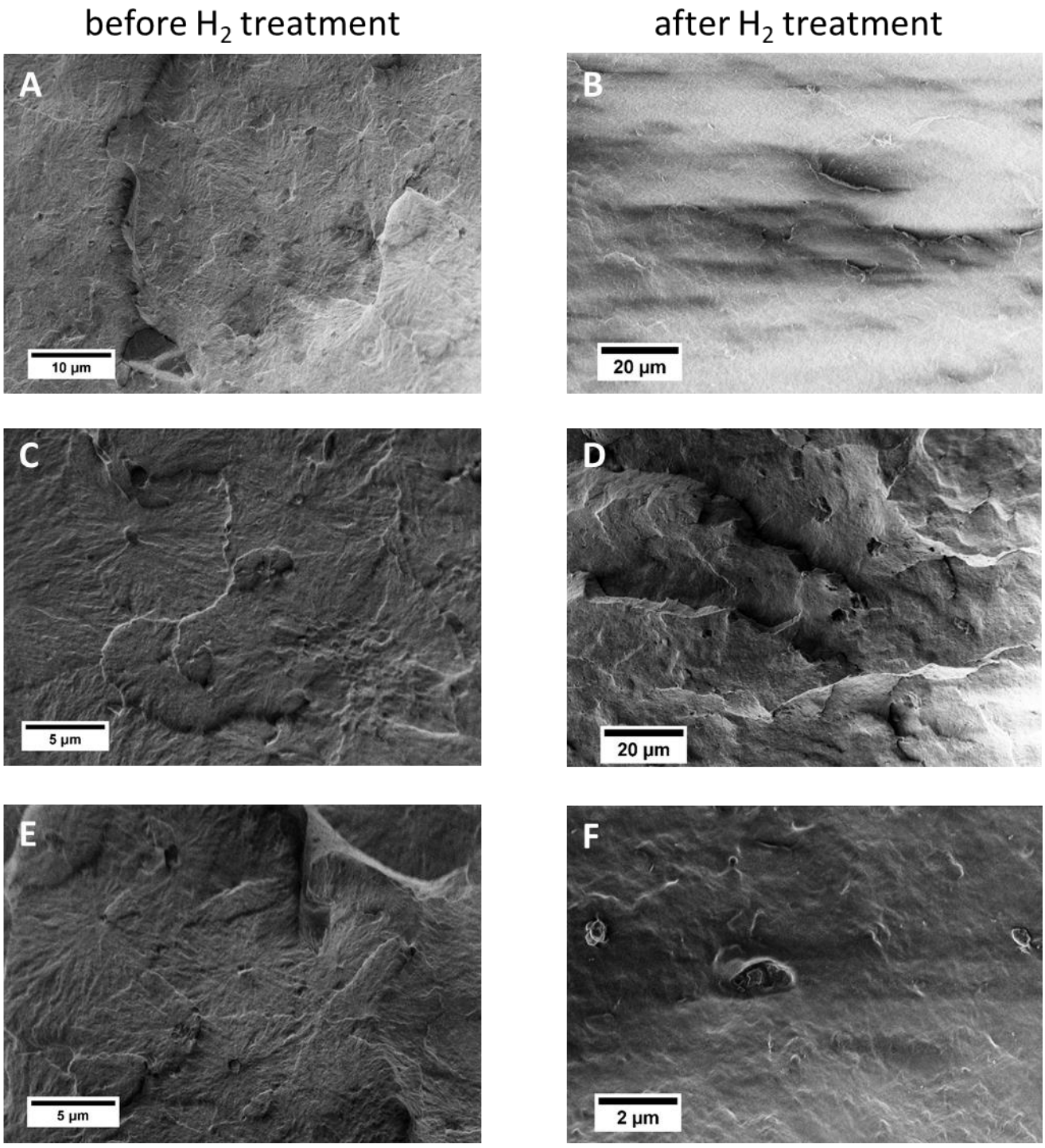


**Figure 3.8.** Scanning electron microscopy (SEM) images of the freeze fracture surface of sample FAT_004 (PU) before (A, C, E) and after hydrogen incubation (B, D, F) shown at different magnifications.[4]

[4] Figure modified from Morsbach et al., Hydrogen Compatibility of Polymers for Fuel Cell Vehicles, Energy Technology 2022, 2200018, DOI: 10.1002/ente.202200018 (CC BY 4.0).

Figure 3.7 shows the images of the sample surface of sample FAT_004 (PU) before and after hydrogen incubation. Similar to sample FAT_003, the same indentations were visible, but the hydrogen treatment had no obvious effect on the appearance of the sample surface.

Again, a different behavior was observed in the images of the sample freeze fracture surfaces. In Figure 3.8, the same crystalline domains could be found on the sample material before hydrogen contact, as shown before in figure 3.6. Similarly, after hydrogen treatment, these crystalline domains could not be detected anymore. Taken together, the materials present in samples FAT_003 and FAT_004 behaved in a similar way, meaning that also the overall chemical composition probably did not differ significantly.

Figure 3.9 shows the images taken of the sample surface from sample FAT_005 (FKM) batch 1. Additionally, images were recorded from a second batch after hydrogen incubation, to compare the behavior of two different O-ring lots. The surface of the material shows roughness on the nanometer scale in all cases (before and after hydrogen treatment), indicating the presence of a high amount of particles. Based on the contrast, the particles seemed to be of inorganic origin. The hydrogen treatment did not yield in any significant changes of the material surface.

In figure 3.10, the freeze fracture surfaces of the same samples of FAT_005 are shown. Again, the comparison of two different batches after hydrogen treatment is provided. Also in the fracture surfaces, the high amount of inorganic particles can be seen. However, again no significant effect of the hydrogen treatment could be detected. Additionally, larger micrometer sized crystalline domains became visible in the second batch of the provided O-rings. This strongly indicated a significant degree of batch-to-batch variation regarding the material composition.

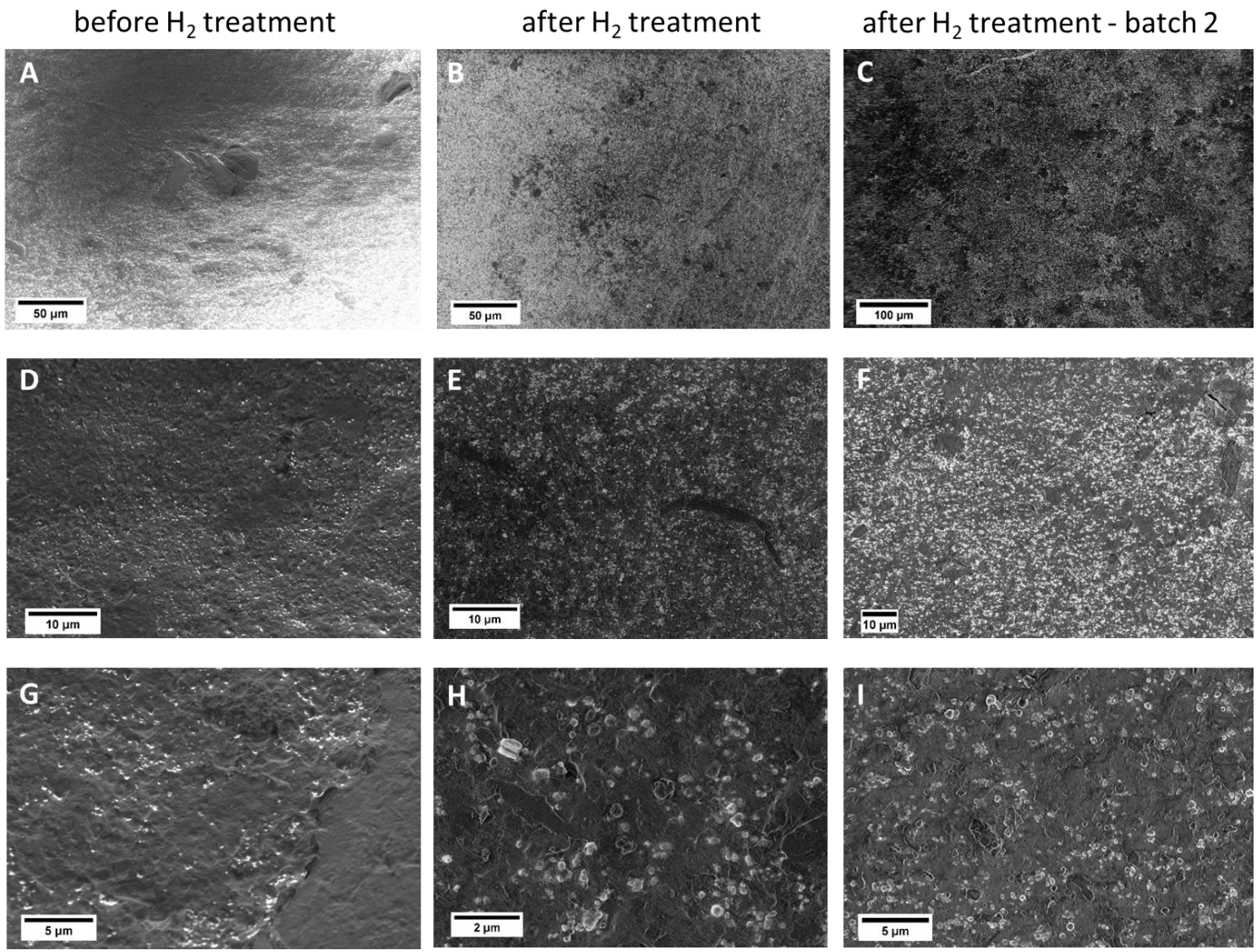


**Figure 3.9.** Scanning electron microscopy (SEM) images of the sample surface of FAT_005 (FKM) before (A, D, G) and after hydrogen incubation (B, E, H) for batch 1 shown at different magnifications. Additionally, images for a second batch (C, F, I) taken after hydrogen incubation are shown.

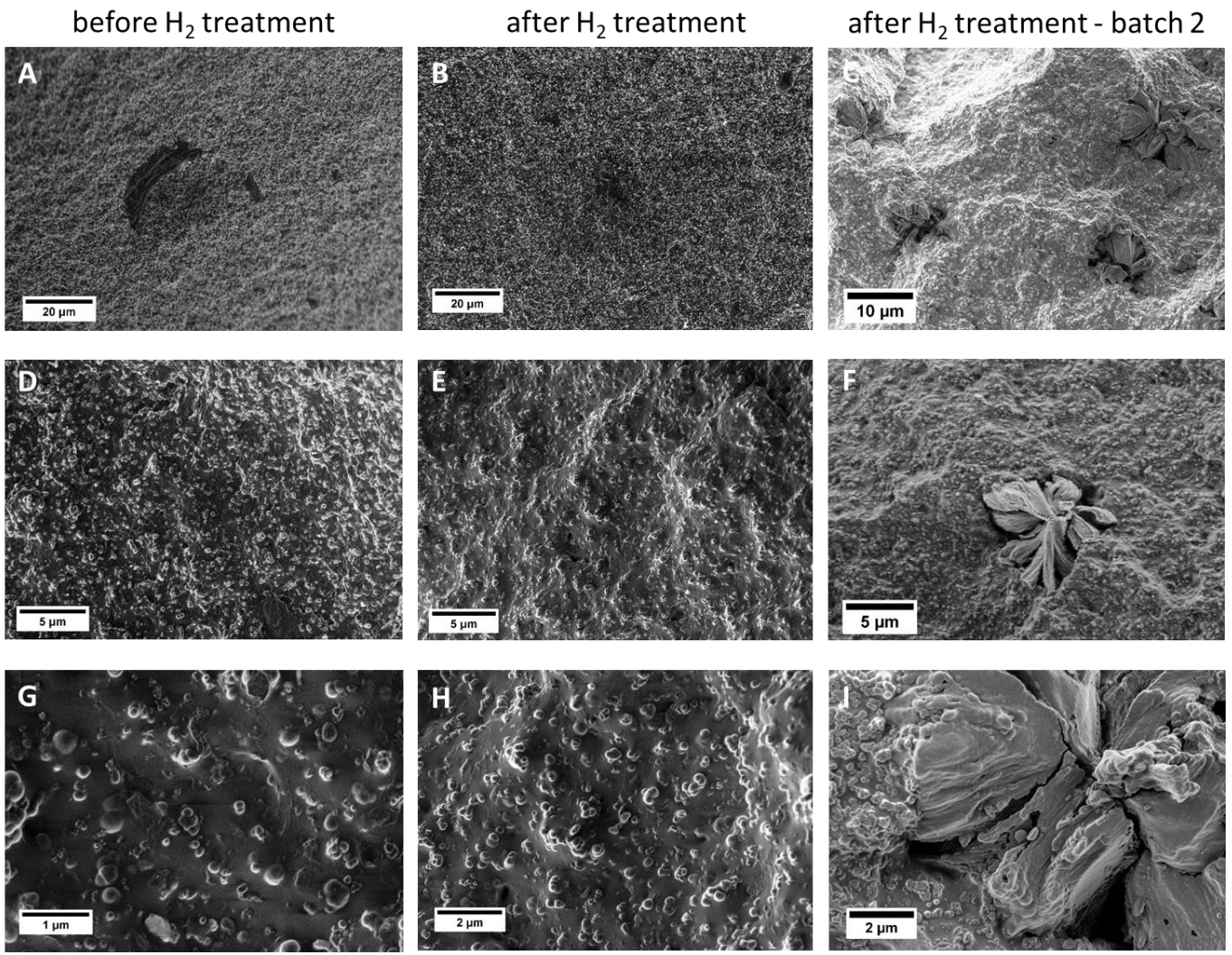


**Figure 3.10.** Scanning electron microscopy (SEM) images of the freeze fracture surface of sample FAT_005 (FKM) before (A, D, G) and after hydrogen incubation (B, E, H) for batch 1 shown at different magnifications. Images for a second batch taken after hydrogen incubation are shown in (C, F, I).

To clarify the nature of present inorganic particles in the sample FAT_005, additionally EDX spectra were recorded from the areas imaged via SEM. The obtained results before and after hydrogen contact, as well as for the second sample batch are shown in figures 3.11, 3.12 and 3.13, respectively.

In the spectra recorded for FAT_005 batch 1 significant amounts of carbon and fluorine could be detected, which can be expected for the FKM material. Additionally, especially co-located with the detected particles, high amounts of oxygen and zinc were detected, suggesting zinc oxide as an inorganic filler material. Again, no significant changes related to the incubation with hydrogen could be found. Regarding the composition of the O-ring from batch 2, the same organic elemental composition was found. However, the inorganic components in that case was found to be calcium instead of zinc, suggesting a different filler material. From the conducted measurements, it is not clear how the change of the inorganic filler material might affect the stability against hydrogen, but it strongly indicates that results from one batch should be verified across different lots.

In summary, the conducted SEM measurements indicate that sample imaging is a very useful tool to obtain a first idea about the morphological changes associated with hydrogen treatments. Ideally, it should be ensured that the same sample specimen is used for imaging before and after the incubation to rule out potential differences stemming from the manufacturing process. Electron microscopy provides a very detailed view on the samples, but is rather demanding in terms of resources. Other microscopy methods might provide easier access to fast imaging, but not be suitable for very precise analysis.



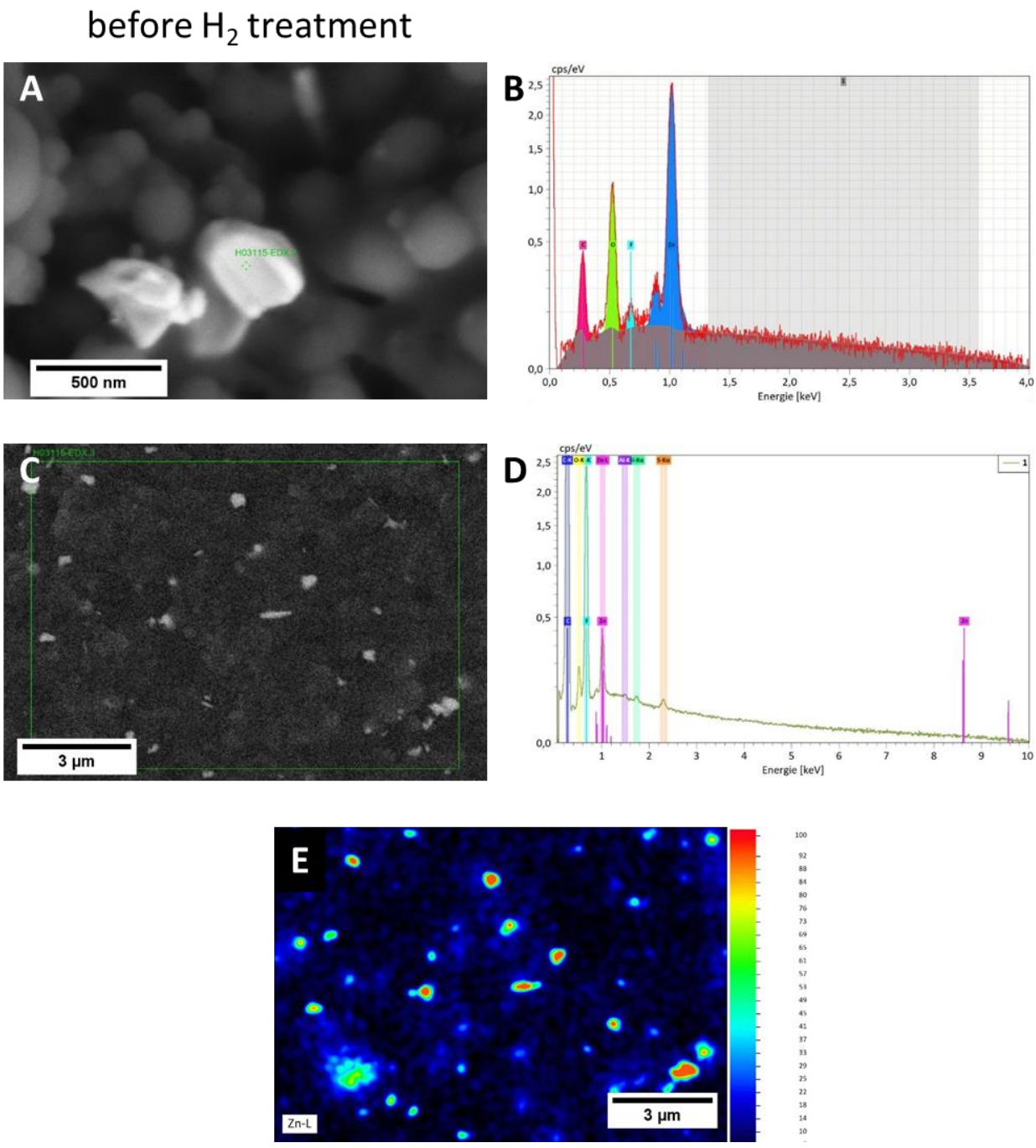


**Figure 3.11.** Scanning electron microscopy (SEM) images of the freeze fracture surface of sample FAT_005 (FKM) batch 1 before hydrogen incubation together with results from EDX analysis. A) Image of analyzed sample area with the spot marked for recording of EDX spectrum in green. B) EDX spectrum corresponding to spot EDX1 marked in A). C) Overview of sample area used for recording of EDX spectrum and heatmap. D) EDX spectrum corresponding to sample area shown in C). E) Heatmap of the detection of Zn in the sample area shown in C).

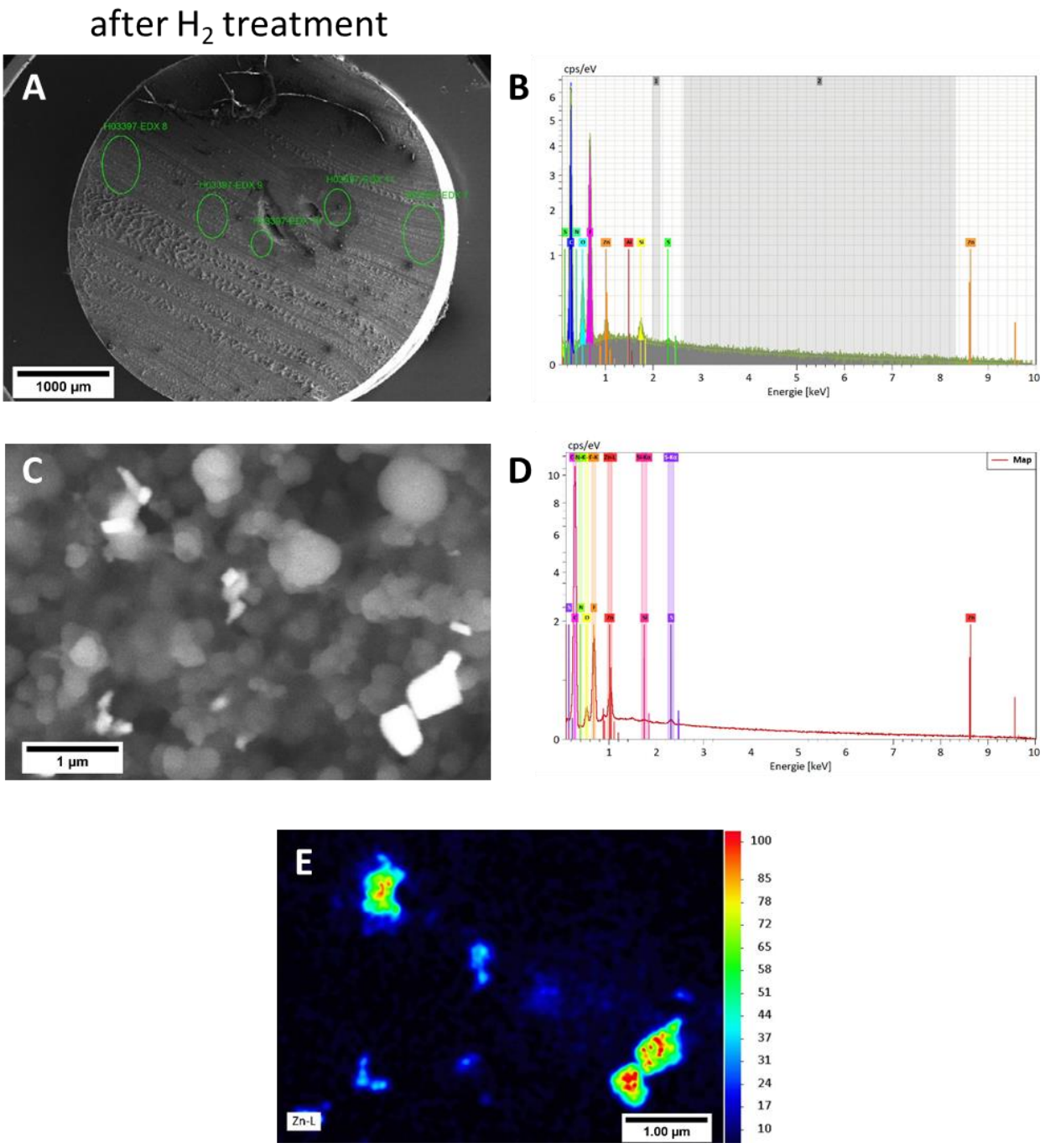


**Figure 3.12.** Scanning electron microscopy (SEM) images of the freeze fracture surface of sample FAT_005 (FKM) batch 1 after hydrogen incubation together with results from EDX analysis. A) Image of analyzed sample area with the spots marked for recording of EDX spectrum in green. B) EDX spectrum corresponding to spot EDX7 marked in A). C) Overview of sample area used for recording of EDX spectrum and heatmap. D) EDX spectrum corresponding to sample area shown in C). E) Heatmap of the detection of Zn in the sample area shown in C).

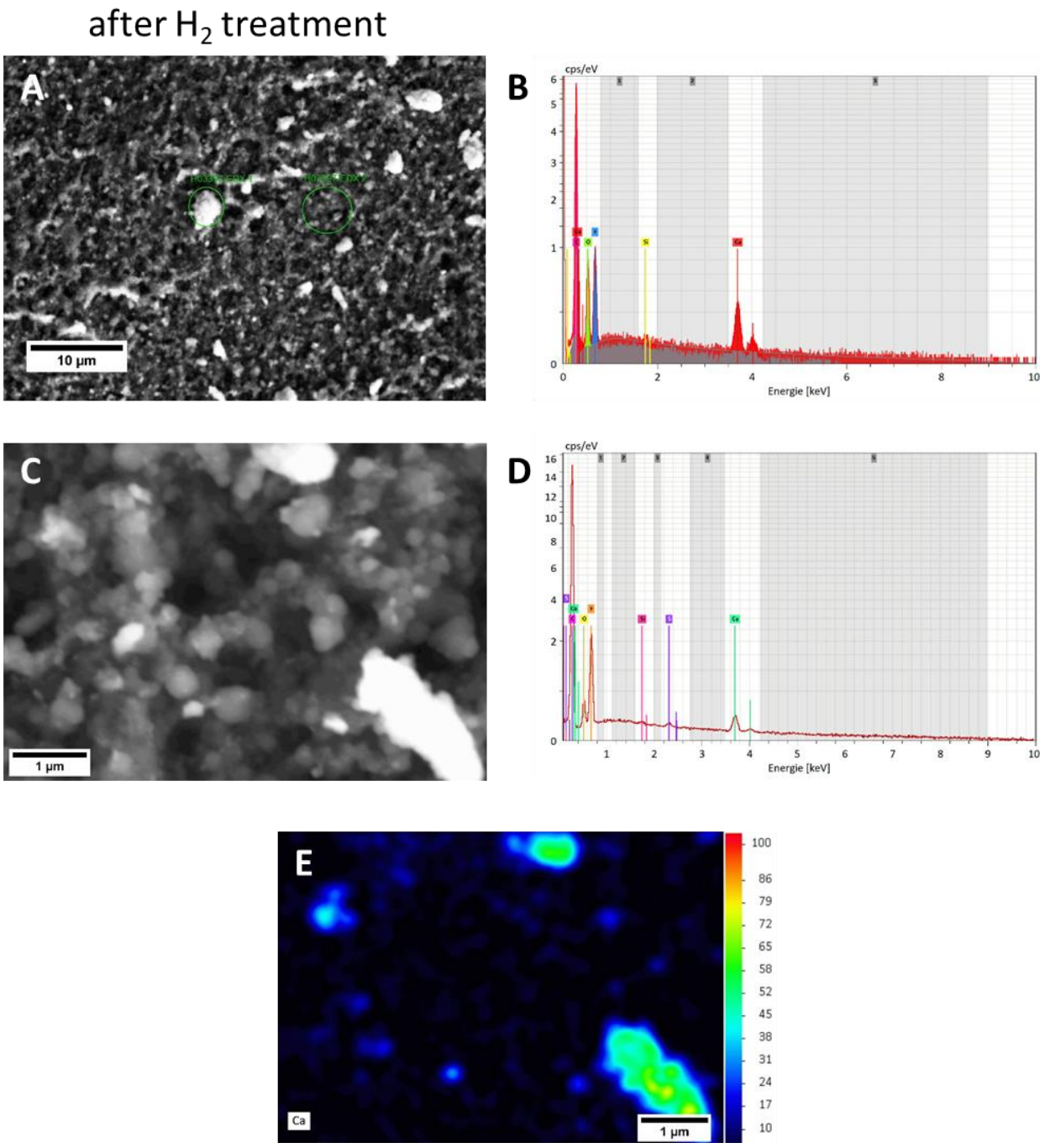


**Figure 3.13.** Scanning electron microscopy (SEM) images of the freeze fracture surface of sample FAT_005 (FKM) batch 2 after hydrogen incubation together with results from EDX analysis. A) Image of analyzed sample area with the spots marked for recording of EDX spectrum in green. B) EDX spectrum corresponding to spot EDX1 marked in A). C) Overview of sample area used for recording of EDX spectrum and heatmap. D) EDX spectrum corresponding to sample area shown in C). E) Heatmap of the detection of Ca in the sample area shown in C).

## 3.2 Chromatographic characterization

For all samples, which show sufficient solubility in a solvent suitable for chromatography, characterization of the relative molecular weights can be performed by gel permeation chromatography (GPC). For the obtained samples, this was the case for TPU and PU samples, which were soluble or partly soluble in tetrahydrofuran (THF). The first sample FAT_001 (TPU) was completely soluble at room temperature before and after $H_2$ incubation and yielded monomodal size distribution curves (see figure 3.14). The molecular weight was calculated relative to linear polystyrene standards and is shown in table 3.1 for comparison.

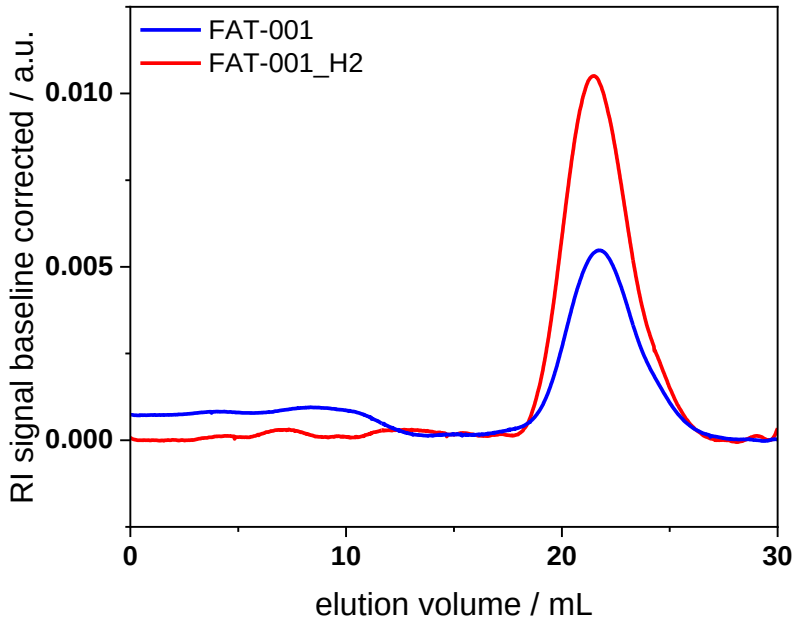


**Figure 3.14.** GPC elution profile of FAT_001 (TPU) in THF before (blue line) and after $H_2$ incubation (red line).

**Table 3.1.** Molecular weight properties of FAT_001 (TPU) determined via GPC in THF before and after $H_2$ incubation.

| | Before $H_2$ incubation | After $H_2$ incubation |
|---|---|---|
| $M_n$ / g mol$^{-1}$ | 68,500 | 81,000 |
| $M_w$ / g mol$^{-1}$ | 133,400 | 143,400 |
| $Đ$ | 1.95 | 1.77 |

According to the elution profile and obtained molecular weights, no significant change could be detected due to the $H_2$ treatment. Variations of the parameters are within accuracy of the method. Since the sample was completely soluble before and after the treatment, it is safe to conclude that the majority of the sample mass did not change regarding the polymer chain lengths and distribution.

The second sample FAT_003 (PU) was only partly soluble at room temperature before $H_2$ incubation (for the insoluble part, sample swelling was visible). After $H_2$ incubation, the solubility increased but still the sample was not fully soluble. In both cases, the soluble part was filtered and measured. The GPC measurement again yielded monomodal size distribution curves (see figure 3.15). The molecular weight was again calculated relative to linear polystyrene standards and is shown in table 3.2 for comparison.

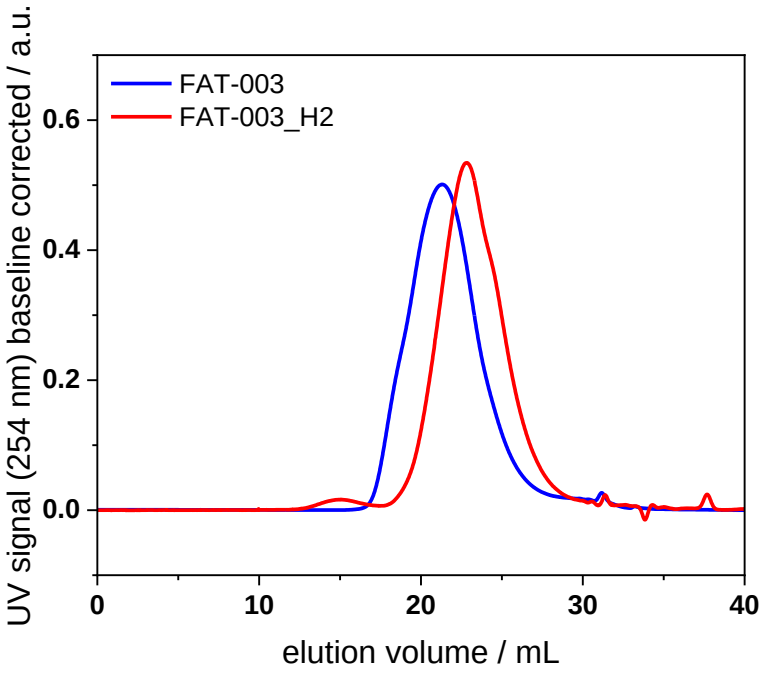


**Figure 3.15.** GPC elution profile of FAT_003 (PU) in THF before (blue line) and after $H_2$ incubation (red line).

**Table 3.2.** Molecular weight properties of FAT_003 (PU) determined via GPC in THF before and after $H_2$ incubation.

| | Before $H_2$ incubation | After $H_2$ incubation |
|---|---|---|
| $M_n$ / g mol$^{-1}$ | 53,500 | 34,900 |
| $M_w$ / g mol$^{-1}$ | 214,000 | 85,700 |
| $Đ$ | 4.00 | 2.45 |

From the elution profiles in figure 3.15, it can be seen that the molecular weight of the soluble fraction of PU changed significantly. After $H_2$ treatment, the molecular weights are substantially smaller than before the treatment (higher elution times = lower molecular weight). This is supported by the calculated molecular weight values, which are approximately decreased by half after the treatment. Since the change is substantial, it can be assumed that a change occurred throughout the whole material, which is in line with the observations made during morphological characterization. However, it should be noted that only the soluble fraction of the sample was characterized, so that information about changes in the non-soluble fraction could not be obtained. As it is unlikely that substantial changes in the chemical structure have occurred, the obtained differences might mainly result from a different solubility behavior due to physical/physico-chemical changes like broken down polymer chains or different intermolecular interactions after the compression.

The third sample FAT_004 (PU) was also only partly soluble at room temperature before $H_2$ incubation (for the insoluble part, sample swelling was visible). After $H_2$ incubation, the solubility remained roughly similar. In both cases, the soluble part was filtered and measured. The GPC measurement yielded size distribution curves with several peaks (see figure 3.16), but with very low UV signal. For the molecular weight determination, only the high $M_w$ peak was evaluated as the other peaks do not represent polymer material. The molecular weight was again calculated relative to linear polystyrene standards and is shown in table 3.3 for comparison.

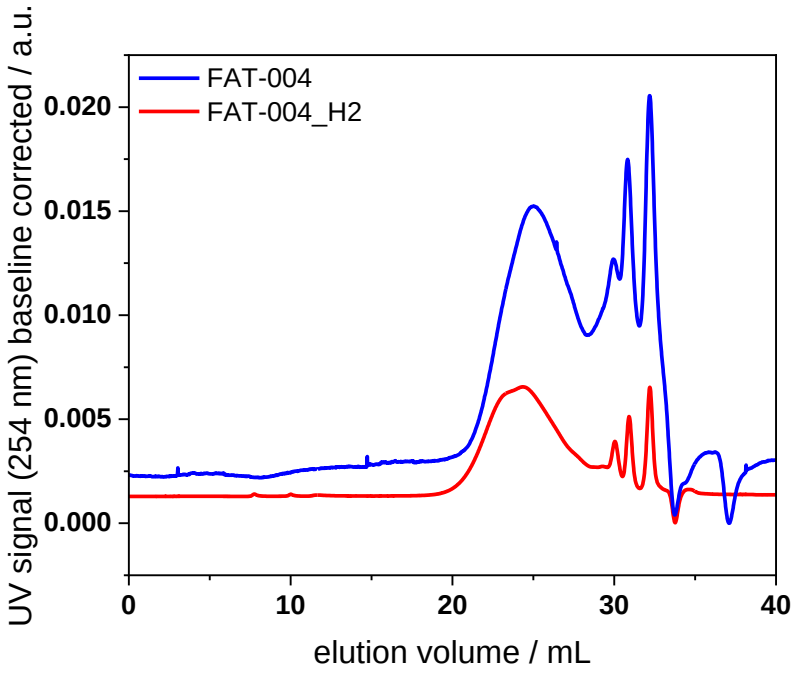


**Figure 3.16.** GPC elution profile of FAT_004 (PU) in THF before (blue line) and after $H_2$ incubation (red line).

**Table 3.3.** Molecular weight properties of FAT_004 (PU) determined via GPC in THF before and after $H_2$ incubation.

| | Before $H_2$ incubation | After $H_2$ incubation |
|---|---|---|
| $M_n$ / g mol$^{-1}$ | 15,700 | 21,615 |
| $M_w$ / g mol$^{-1}$ | 31,800 | 48,115 |
| $Đ$ | 2.03 | 2.23 |

Viewing the elution profiles shown in figure 3.16, no significant differences between the samples FAT_004 before and after $H_2$ incubation were found. For both samples, very low molecular weight species could be detected along with the main polymer peak. These low $M_w$ peaks were outside of the calibration curve and ran into the solvent peaks. Thus, they probably result from small molecule additives with high UV activity. The molecular weight values listed in table 3.3 are similar within the accuracy of the measurement.

For the samples FAT_002 (PEEK) and FAT_005 (FKM), no suitable sample preparation for GPC

could be performed. Depending on the material properties, PEEK can be dissolved in hot dichloroacetic acid and then diluted with chloroform to obtain a final sample concentration of 2 g/L. Then, the sample can be injected and measured with an eluent containing 80 vol% chloroform and 20 vol% dichloroacetic acid.[1] However, in this case, no solubility in hot dichloroacetic acid was achieved for FAT_002 before and after $H_2$ incubation, so that characterization via GPC was not possible. Similarly, fluoroelastomers can in principle be dissolved in DMF containing 1 g/L LiBr at elevated temperatures (in this case 80 °C) and measured in the same solvent.[2] Also for this procedure, no significant solubility could be achieved for the samples under investigation (FAT_005) before and after $H_2$ incubation.

In summary, it can be concluded that GPC is a valid method to determine material changes after $H_2$ treatment as long as sample solubility in the desired solvents can be achieved. Then, detected molecular weight changes can give hints about the processes taking place during the treatment. For example, a decrease of the molecular weight as observed for FAT_003, suggests a polymer degradation taking place to a certain extent or a changed material solubility due to the compression during the incubation process. To clarify whether these changes are a result of contact to hydrogen or also occur in other atmospheres, control experiments should be performed. For materials that possess a high stability against any kind of solvent or other aggressive chemicals, GPC is not a method of choice to evaluate material properties.

## 3.3 Thermal characterization

Thermal characterization methods give important hints about the properties of a polymer material and allow conclusions about its structure. Accordingly, in thermogravimetric analysis (TGA), the decomposition temperatures and associated mass loss of polymers can be determined in different gas atmospheres. Like this, the role of e.g. oxygen during the decomposition can be assessed. In addition, thermal conversions can be detected with differential scanning calorimetry (DSC) – including melting points and glass transition temperatures. These characteristic material properties depend highly on the chemical structure and crystallinity in the sample.

Thus, each sample was first subjected to TGA and to DSC analysis as described in the experimental section. The obtained TGA results for sample FAT_001 (TPU) before and after $H_2$ incubation are shown in figure 3.17 and table 3.4.

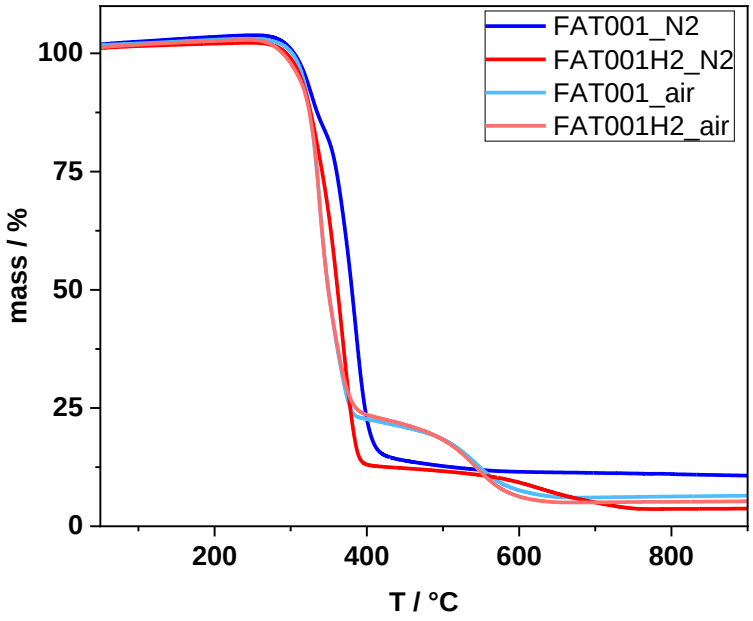


**Figure 3.17.** TGA curves of FAT_001 (TPU) before and after $H_2$ incubation measured in $N_2$ or synthetic air atmosphere normalized to initial sample mass.

**Table 3.4.** Detected decomposition steps and associated mass loss in TGA for FAT_001 as determined from inflection points of thermograms reported in figure 3.17. Significant changes after $H_2$ incubation are marked in light red for clarity.

| | Decomposition steps | Before $H_2$ incubation | After $H_2$ incubation |
|---|---|---|---|
| $N_2$ | $T_1$ (assoc. mass loss) | 339 °C (19%) | 368 °C (88%) |
| | $T_2$ (assoc. mass loss) | 388 °C (71%) | 622 °C (8%) |
| Air | $T_1$ (assoc. mass loss) | 339 °C (77%) | 336 °C (78%) |
| | $T_2$ (assoc. mass loss) | 549 °C (16%) | 547 °C (17%) |

From the obtained thermograms, it can be observed that FAT_001 shows two distinct decomposition steps in $N_2$ as well as in air. In $N_2$, these steps are significantly different after incubation in $H_2$, while in air they remain unchanged. In general, the material properties of TPU depend highly on the nature of hard and soft segments in the polymer. The hard segment is usually composed of the diisocyanate component, which can be aromatic or aliphatic. The soft segment is more variable and contains the

diol component, which is mostly introduced as a polyol (polyether or polyester depending on application) and can vary in chain length. The decomposition processes occurring are accordingly influenced by the ratio and chemical structure of hard and soft segment as well as the type of polyol used. During thermal degradation, the urethane bond can degrade in various ways involving e.g. the dissociation into isocyanate and alcohol or the elimination of $CO_2$ yielding a primary or secondary amine. In literature, degradation ranges of ~300 to ~450 °C are reported in $N_2$, with higher degradation temperatures for TPU with higher fractions of hard segments.[3-6] This is also the case for the examined sample FAT_001, which exhibits two degradation steps in this range. According to the given literature references, the first step corresponds mainly to the liberation of $CO_2$, while in the second step $H_2O$, HCN and other small molecules might be released. In synthetic air, an additional degradation step between 500-600 °C was reported previously, which is also in line with the here obtained results.[3] This step presumably corresponds to further decomposition of the previously formed char in the presence of oxygen. After $H_2$ incubation, only one degradation step was observed under $N_2$ for FAT_001, which could indicate that the two previous decomposition processes took place at similar temperature due to a changed nature of the segments or that the type of decomposition reaction has changed. Both scenarios include the precondition that changes throughout the material occurred. Additionally, a new degradation step at even higher temperatures occurred (>600 °C), leading to an overall higher mass loss (96%) vs. the thermal degradation before $H_2$ treatment (90%).

Next, the samples were analyzed with DSC as shown in Figure 3.18. In both samples, a similar heating curve was obtained, yielding a glass transition temperature $T_g$ of -47 °C. A $T_g$ below 0 °C can be attributed to the soft segment of the polymer, while potential glass transition temperatures of the hard segment should occur at much higher temperatures.[4-6] In addition, the change in heat capacity $\Delta c_p$ can be determined for the glass transition points. For FAT_001, values of 0.477 J $g^{-1}$ $K^{-1}$ before and 0.656 J $g^{-1}$ $K^{-1}$ after hydrogen incubation were obtained, which presents a significant difference. Generally, lower $\Delta c_p$ values indicate a higher degree of crystallinity throughout the sample. Without exact knowledge about the chemical composition it is, however, very hard to interpret the obtained changes. Finally, other significant phase transitions than the $T_g$ at low temperatures could not be observed indicating a high crystallinity of the hard segment. Thus, we cannot conclude anything about changes occurring during $H_2$ treatment in the hard segment.

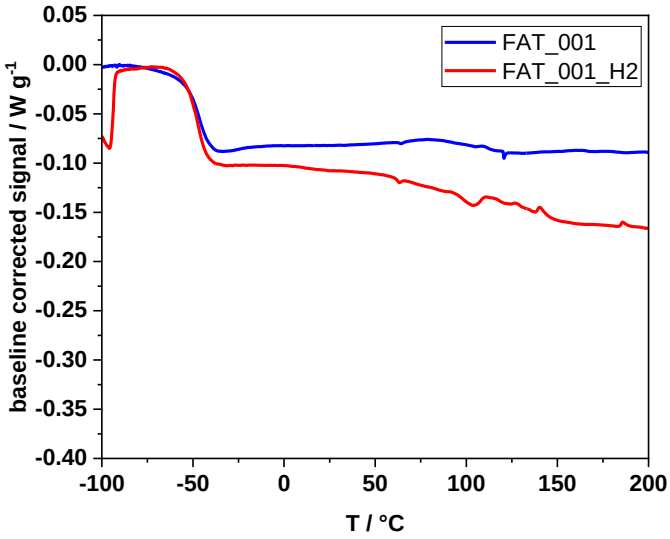


**Figure 3.18.** DSC melting curves (heat rate 10 K $min^{-1}$) of FAT_001 (TPU) before (blue) and after $H_2$ incubation (red).

Similar to the analysis of sample FAT_001, also the PEEK material (FAT_002) was subjected to TGA measurements. Figure 3.19 shows the obtained decomposition curves before and after hydrogen incubation under different atmosphere. Temperatures and associated mass loss of each decomposition step are listed in table 3.5. PEEK in general shows two distinct decomposition steps independent from the different conditions. Under $N_2$ atmosphere, a significant amount of char formation was observed, meaning that roughly only 50% of mass loss was detected. This behavior corresponds to the observations reported in literature and is a result of the high degree of aromatic groups in the main polymer chain.[7] The onset of decomposition generally occurred roughly from 575 °C on. As a main mechanism degradation during the first decomposition step, random chain scission of ether and ketone bonds reported. Products of this step are mainly phenol, CO and $CO_2$.[8, 9] At higher temperatures under $N_2$, the formation of radical intermediates and further decomposition of these was reported. In air, the second decomposition step is attributed to oxidation of the carbonaceous char formed in the first decomposition step. Comparing the materials before and after $H_2$ treatment, the only significant change that was found, corresponds to a higher stability of the material under $N_2$ in the second decomposition step. Here, less mass loss was detected at a higher decomposition temperature. The reason for this effect has to be further examined in additional experiments.

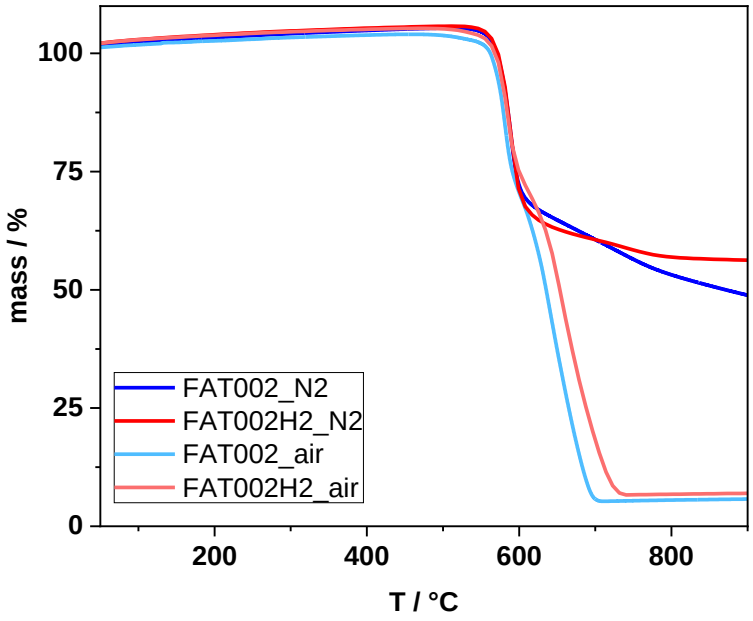


**Figure 3.19.** TGA curves of FAT_002 (PEEK) before and after $H_2$ incubation measured in $N_2$ or synthetic air atmosphere normalized to initial sample mass.

**Table 3.5.** Detected decomposition steps and associated mass loss in TGA for FAT_002 as determined from inflection points of thermograms reported in Figure 3.19.

| | Decomposition steps | Before $H_2$ incubation | After $H_2$ incubation |
|---|---|---|---|
| $N_2$ | $T_1$ (assoc. mass loss) | 592 °C (35%) | 592 °C (39%) |
| | $T_2$ (assoc. mass loss) | 650 °C (16%) | 727 °C (4%) |
| Air | $T_1$ (assoc. mass loss) | 589 °C (31%) | 589 °C (31%) |
| | $T_2$ (assoc. mass loss) | 653 °C (63%) | 659 °C (62%) |

Subsequently, thermal conversions occurring the sample were analysed via DSC. In figure 3.20, the melting curves before and after hydrogen incubation are shown. In both experiments, one main phase transition, corresponding to a melting point of 339 °C before and 340 °C after the treatment, was observed. This exactly matches the literature reported melting point of 339 °C determined at 10 K $min^{-1}$.[10] Here, it can be concluded that the thermal properties of the material were not affected by the hydrogen incubation procedure.

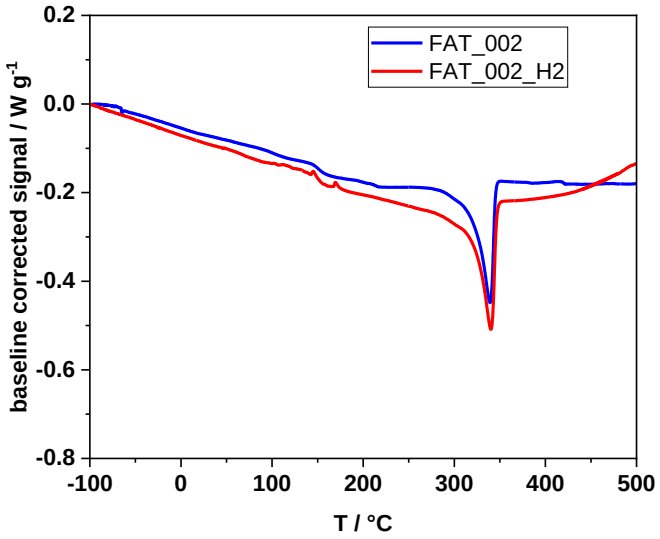


**Figure 3.20.** DSC melting curves (heat rate 10 K $min^{-1}$) of FAT_002 (PEEK) before (blue) and after $H_2$ incubation (red).

As described above, TGA measurements were next performed on the sample FAT_003 (PU). The obtained decomposition curves are shown in figure 3.21 together with the corresponding temperatures and mass loss fractions in table 3.6. Generally, similar degradation steps and temperatures as for sample FAT_001 were found. Degradation under $N_2$ took place in two distinct decomposition steps as seen before in a temperature range between 300-450 °C. In air, a third step could be detected. Changes due to the hydrogen incubation are mainly visible in the measurements under $N_2$ atmosphere. Here, significantly less mass loss was found during the first decomposition step, leading to an overall mass loss of only 70% versus 92% before the hydrogen treatment. Minor differences can also be found in the high temperature regime under air, referring to the number of distinguishable steps. Interestingly, these measurements suggest a higher thermal stability of the material after hydrogen incubation.

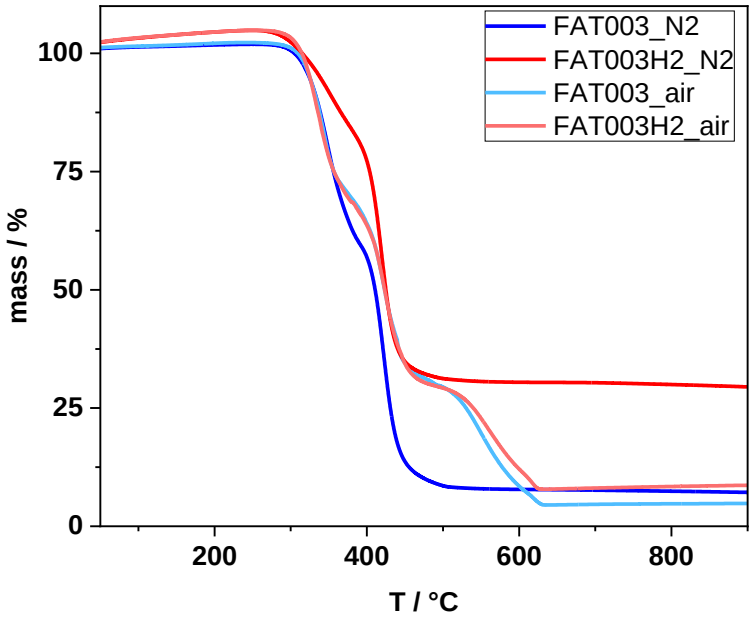


**Figure 3.21.** TGA curves of FAT_003 (PU) before and after $H_2$ incubation measured in $N_2$ or synthetic air atmosphere normalized to initial sample mass.

**Table 3.6.** Detected decomposition steps and associated mass loss in TGA for FAT_003 as determined from inflection points of thermograms reported in Figure 3.21.

| | Decomposition steps | Before $H_2$ incubation | After $H_2$ incubation |
|---|---|---|---|
| $N_2$ | $T_1$ (assoc. mass loss) | 348 °C (40%) | 353 °C (15%) |
| | $T_2$ (assoc. mass loss) | 425 °C (52%) | 421 °C (55%) |
| Air | $T_1$ (assoc. mass loss) | 347 °C (31%) | 341 °C (32%) |
| | $T_2$ (assoc. mass loss) | 448 °C (39%) | 427 °C (39%) |
| | $T_3$ (assoc. mass loss) | 555 °C (25%) | 559 °C (18%) |
| | $T_4$ (assoc. mass loss) | - | 621 °C (3%) |

Again, the sample FAT_003 was subjected to thermal analysis via DSC. The obtained melting curves are shown in figure 3.22. Both melting curves before and after hydrogen incubation show a very similar thermal behavior. As a main phase transition, a glass transition point at -68°C and -71 °C, respectively, was detected, which is also in line with the $T_g$ determined for FAT_001. Also, the change

of heat capacity $\Delta c_p$ was determined and yielded values of 0.332 J $g^{-1}$ $K^{-1}$ before and 0.342 J $g^{-1}$ $K^{-1}$ after hydrogen treatment, which can be considered as similar. This means that, within the accuracy of the measurement, no significant changes of the thermal properties were found. Several other minor phase transitions were detected as well, probably resulting from additives. These were as well similar under both conditions.

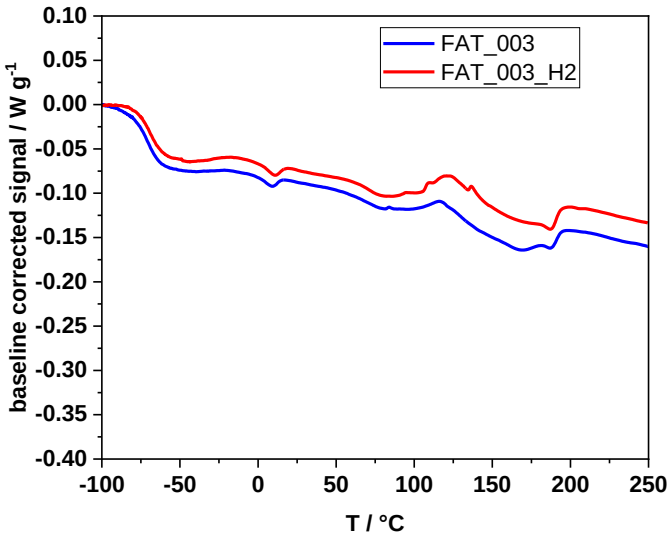


**Figure 3.22.** DSC melting curves (heat rate 10 K $min^{-1}$) of FAT_003 (PU) before (blue) and after $H_2$ incubation (red).

FAT_004 was analysed as a next step similar to FAT_003 being composed of the same sample material. The temperature range of detected decomposition steps shown in figure 3.23 and table 3.7 corresponds to the one detected for FAT_003, but the individual steps took place at slightly different temperatures with different associated mass loss. This indicates a different chemical composition of the PU material. Indeed, the decomposition profile is more similar to the one of FAT_001. Changes after hydrogen incubation were only recorded in synthetic air atmosphere. Also here, decomposition steps two and three were shifted to slightly higher temperatures with less overall mass loss, corresponding to a higher thermal stability of the material.

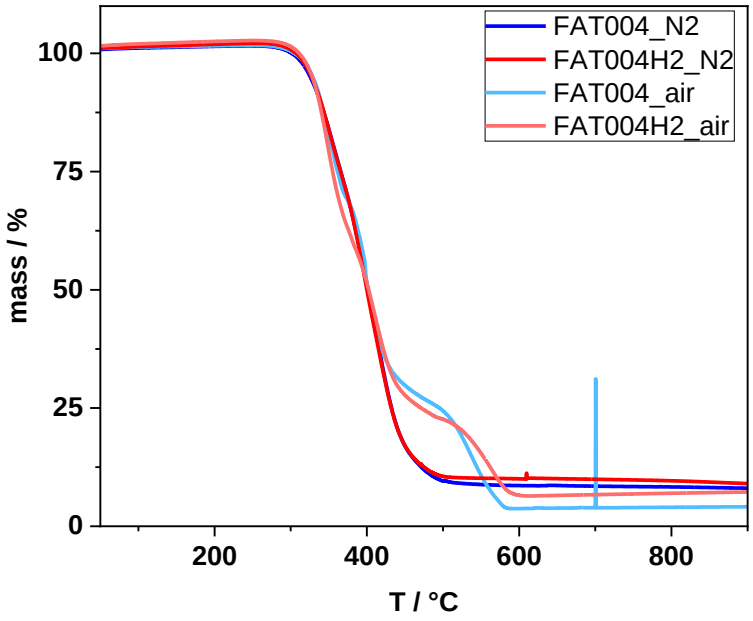


**Figure 3.23.** TGA curves of FAT_004 (PU) before and after $H_2$ incubation measured in $N_2$ or synthetic air atmosphere normalized to initial sample mass.

**Table 3.7.** Detected decomposition steps and associated mass loss in TGA for FAT_004 as determined from inflection points of thermograms reported in figure 3.23.

| | Decomposition steps | Before $H_2$ incubation | After $H_2$ incubation |
|---|---|---|---|
| $N_2$ | $T_1$ (assoc. mass loss) | 356 °C (28%) | 355 °C (26%) |
| | $T_2$ (assoc. mass loss) | 406 °C (64%) | 400 °C (65%) |
| Air | $T_1$ (assoc. mass loss) | 360 °C (31%) | 348 °C (37%) |
| | $T_2$ (assoc. mass loss) | 405 °C (42%) | 415 °C (36%) |
| | $T_3$ (assoc. mass loss) | 544 °C (23%) | 569 °C (16%) |

DSC analysis of the sample FAT_004 yielded the thermal sample properties before and after hydrogen incubation shown in figure 3.24. As expected, also in this material glass transition temperatures of -55 °C and -52 °C, respectively, were recorded. The change of heat capacity $\Delta c_p$ was determined to be 0.278 J $g^{-1}$ $K^{-1}$ before and 0.159 J $g^{-1}$ $K^{-1}$ after hydrogen incubation, presenting a significant difference regarding the sample crystallinity. However, from the morphological

characterization, the opposite trend could have been expected (lower crystallinity after incubation). Additionally, as another main phase transition, a melting point of 229 °C before and 230 °C after hydrogen treatment was determined. Again, for all phase transitions, no influence of the hydrogen incubation was found.

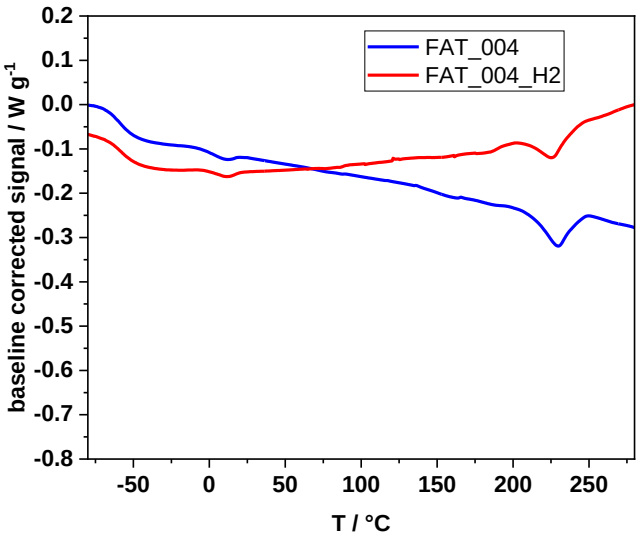


**Figure 3.24.** DSC melting curves (heat rate 10 K $min^{-1}$) of FAT_004 (PU) before (blue) and after $H_2$ incubation (red).

As a last sample, FAT_005 composed of FKM material was analysed regarding the decomposition steps upon thermal treatment. Corresponding curves are shown in figure 3.25 together with the recorded values in table 3.8. For this type of material, three different decomposition steps were found under $N_2$ as well as under air atmosphere. The main step under $N_2$ was the second decomposition step, while under air, the third step introduced another significant part of degradation reactions. In literature, usually one single decomposition step in $N_2$ is reported in the range of 430 – 500 °C, depending on the monomer composition. [11, 12] The occurring degradation processes are described to be very complex, but can generally be divided in to two main routes: decomposition of chain carbon bonds (main) and decomposition by splitting off hydrogen and fluorine as HF (secondary).[13] During thermal treatment, the oxidation of C-F bonds might take place in the presence of oxygen as described in literature.[14] This could lead to the generation of carboxylic groups and subsequently further

oxidation to $CO_2$. In the TGA curves shown in figure 3.25, this process might correspond to the third main degradation step in synthetic air.

Changes after hydrogen treatment were not found for the degradation under $N_2$, but for the decomposition in the high temperature regime under air, indicating that the occurring oxidation reactions might have changed. Additionally, the two sample batches received after hydrogen treatment were compared as well, yielding no significant differences in their thermal decomposition behavior.

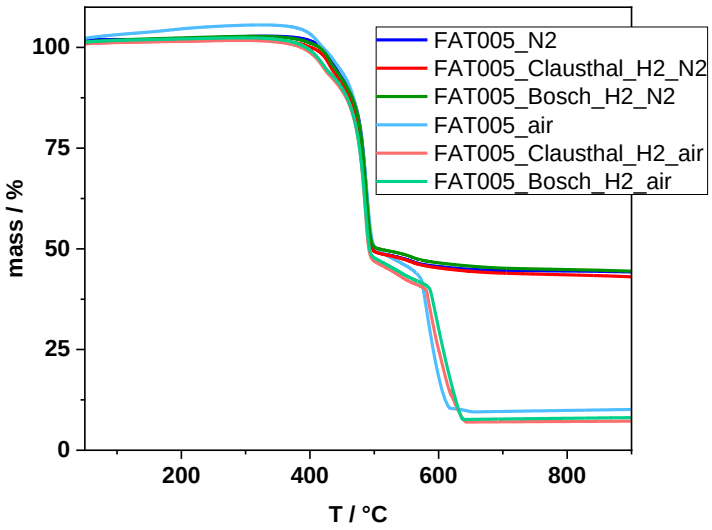


**Figure 3.25.** TGA curves of FAT_005 (FKM) before and after $H_2$ incubation measured in $N_2$ or synthetic air atmosphere normalized to initial sample mass.

**Table 3.8.** Detected decomposition steps and associated mass loss in TGA for FAT_005 as determined from inflection points of thermograms reported in figure 3.25.

| | Decomposition steps | Before $H_2$ inc. | After $H_2$ inc. | After $H_2$ inc. batch 2 |
|---|---|---|---|---|
| $N_2$ | $T_1$ (assoc. mass loss) | 434 °C (8%) | 434 °C (6%) | 434 °C (6%) |
| | $T_2$ (assoc. mass loss) | 491 °C (44%) | 490 °C (45%) | 490 °C (44%) |
| | $T_3$ (assoc. mass loss) | 561 °C (4%) | 561 °C (5%) | 561 °C (5%) |
| Air | $T_1$ (assoc. mass loss) | 440 °C (5%) | 425 °C (7%) | 424 °C (6%) |
| | $T_2$ (assoc. mass loss) | 492 °C (48%) | 491 °C (47%) | 490 °C (47%) |
| | $T_3$ (assoc. mass loss) | 588 °C (37%) | 544 °C (4%) | 544 °C (5%) |
| | $T_4$ (assoc. mass loss) | - | 630 °C (34%) | 605 °C (34%) |

Finally, also the thermal phase transitions occurring in FKM were determined via DSC, before and after hydrogen treatment. As shown in figure 3.26, the main reported phase transition was a glass transition temperature at -54 °C before $H_2$ as well as -54 °C (batch 1) and -53 °C (batch 2) after $H_2$. These temperatures did not change significantly related to the hydrogen incubation. The determination of change in heat capacity $\Delta c_p$ yielded values of 0.148 J $g^{-1}$ $K^{-1}$ before and 0.080 J $g^{-1}$ $K^{-1}$ (batch 1) as well as 0.089 J $g^{-1}$ $K^{-1}$ (batch 2) after hydrogen incubation. Again, a significant decrease was found, which is similar for both obtained batches (assuming a similar value for batch 1 and 2 before incubation). In principle, this indicates again a higher degree of crystallinity in the sample after the treatment. Additionally, after hydrogen contact, a small peak corresponding to a melting point became visible at around 0 °C. However, this peak was very small and is probably not a result of the main polymer material. Other phase transitions occurring might be related to additives used in the O-rings, similar to FAT_003 and FAT_004.

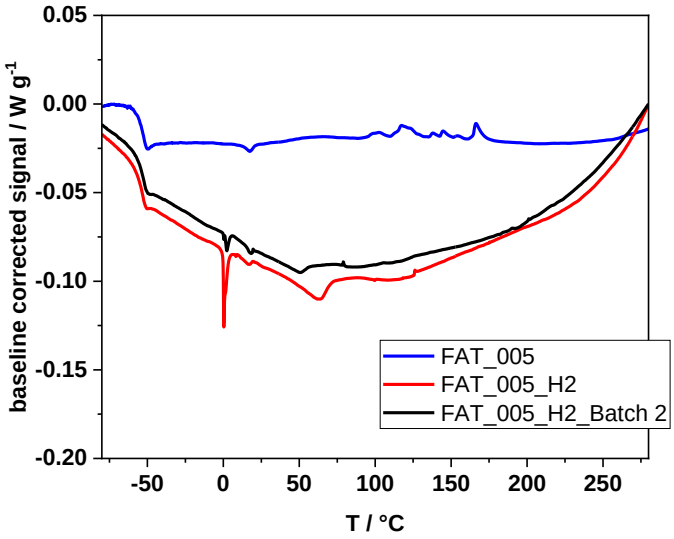


**Figure 3.26.** DSC melting curves (heat rate 10 K $min^{-1}$) of FAT_005 (FKM) before (blue) and after $H_2$ incubation (red). Additionally, the melting curve of a second FAT_005 sample batch after incubation is shown (black).

In summary, the conducted thermal characterization yields valuable information regarding material properties before and after the conducted incubation processes. Occurring changes due to the treatment were only visible by thermogravimetric analysis, which offers a rather fast and convenient way to detect already minor material differences. Further investigations are needed, however, to clarify the nature of these variations. Differential scanning calorimetry on the other side, allows to estimate the influence on material performance based on its physical appearance (mainly the glass transition point). In this study, changes were not detected in these measurements regarding the phase transition temperatures, but the determination of change in heat capacity might present an opportunity for further evaluation. But this is only possible if the chemical structure of the material is known exactly. In general, the method might be valuable as a quality control step regarding the application of the materials.

## 3.4 Characterization of mechanical properties

To assess the influence of hydrogen incubation on the mechanical properties of the materials, different investigations were performed with samples, where enough sample material (at least three identical specimen) was provided. This was the case for FAT_001, FAT_002 and FAT_003. Depending on the sample species, either tensile tests (shouldered test bars) or compression tests (O-rings) were performed. These measurements were done on the basis of the norms DIN 53504 and DIN ISO 815.

For FAT_001, during the tensile tests a significant amount of material elongation was recorded upon drawing of the samples (see figure 3.27). A maximum elongation of ca. 800 % was achieved with a tensile strength of slightly more than 10 MPa. For the flexible TPU material, this was expected to be the case. A comparison of the samples before and after hydrogen incubation show a slight difference, but it was not significant given the variation between samples. However, some hints are obtained that higher stress might be required after hydrogen treatment to achieve the same strain as before. This correlates with the observation that the material might have been irreversibly compressed obtained from SEM. However, to yield meaningful results, the incubation parameters might have to be modified (e.g. longer storage time, higher temperature or pressure) so that changes due to the treatment become more visible.

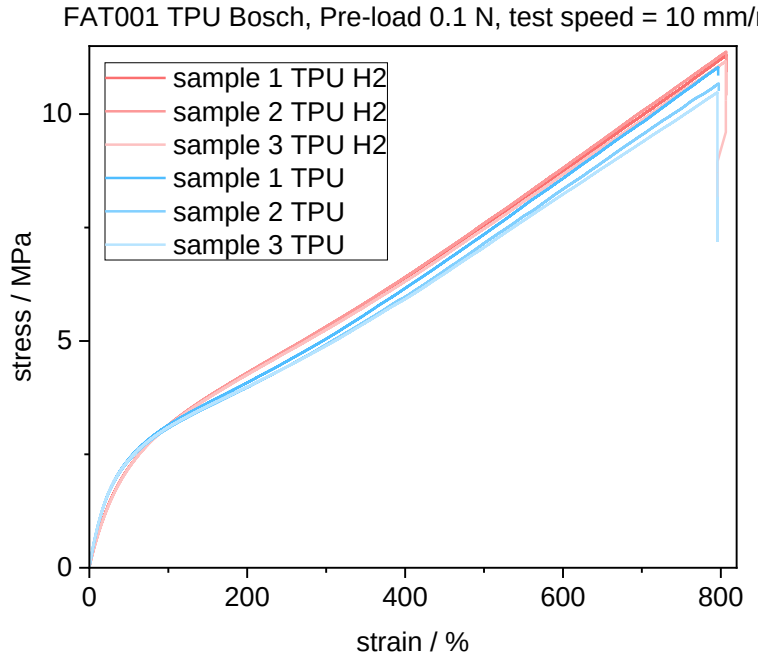


**Figure 3.27.** Stress vs. strain recorded for FAT_001 (TPU) shouldered test bars during tensile tests. Curves are shown for three samples each from material before and after hydrogen incubation.

For FAT_002, stress vs. strain curves were as well recorded during tensile tests as shown in figure 3.28. As PEEK is generally a very hard and stiff material, almost no elongation upon drawing took place. Only a little less than 1% of strain was achieved under the same conditions as for FAT_001. No significant differences were detectable regarding the samples before and after hydrogen treatment.

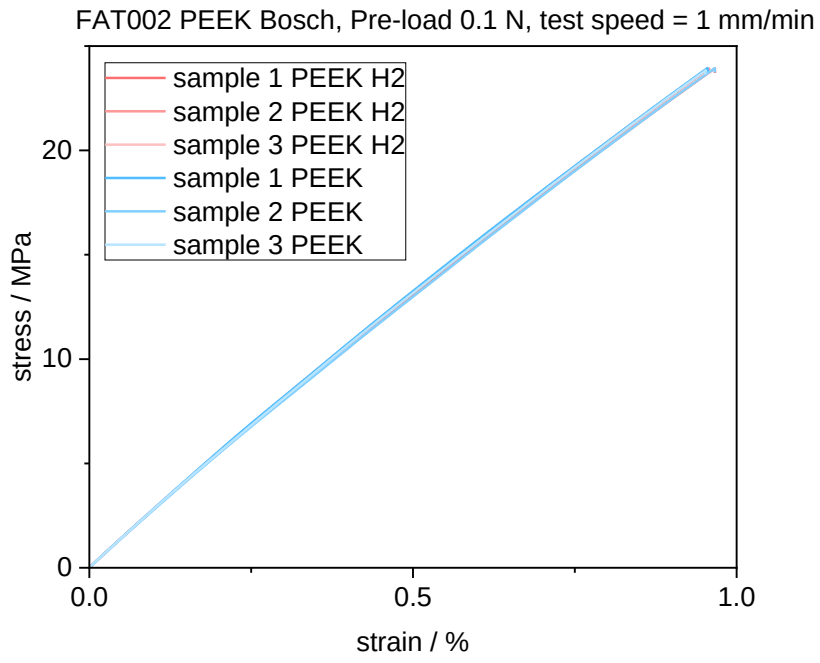


**Figure 3.28.** Stress vs. strain recorded for FAT_002 (PEEK) shouldered test bars during tensile tests. Curves are shown for three samples each from material before and after hydrogen incubation.

For the obtained O-ring samples, the mechanical properties were then recorded during compression tests, which corresponds to the final application to these samples as sealing materials. Figure 3.29 shows the obtained force vs. compression curves recorded from five cycles of three individual O-rings each before and after hydrogen incubation. Samples were compressed up to a compression ratio of 10% and subsequently decompressed again. Also in this case, the variation between individual samples was higher than the difference between samples before and after hydrogen treatment. As such, no significant effect could be detected on the performance of the O-rings.

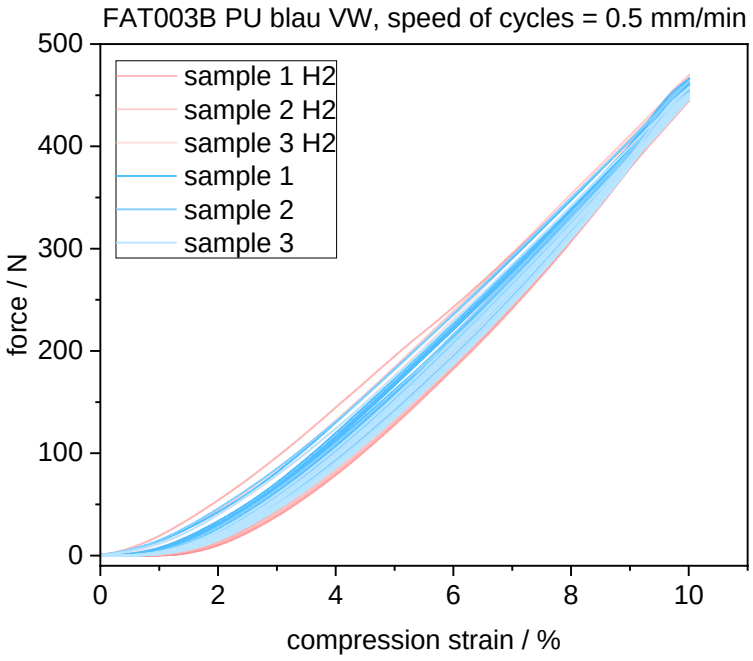


**Figure 3.29.** Force vs. compression strain recorded for FAT_003 (PU) O-rings during compression tests. Curves are shown for three samples each from material before and after hydrogen incubation.

Concluding the rheological testing, the performed measurements were not suitable to detect changes due to hydrogen treatment in this study. This might be due to the fact that present differences were too small to have a significant impact on the overall rheological performance. However, under more severe treatment conditions, these effects might become considerable, so that rheological measurements might present an important quality control tool, especially to assess the sealability of O-rings. In general, the rheological measurements do not require a high amount of resources as tensile and compression tests can be performed with the same device. However, a high amount of sample material is required to yield statistically relevant information.

## 3.5 Chemical analysis (NMR)

To assess changes in the chemical composition of the obtained samples before and after hydrogen treatment, solid state NMR (nuclear magnetic resonance) spectroscopy measurements were performed where possible. For the samples FAT_003 (PU), FAT_004 (PU) and FAT_005 (FKM) enough suitable sample material was available. In all cases, spectra were recorded for the isotopes $^{1}H$ and $^{13}C$.

For the first sample (FAT_003) $^{1}H$ NMR spectra before and after hydrogen treatment are shown in figure 3.31. The main obtained signals correspond to two distinct regions of chemical shift: Signals in the range of δ = 8.5 – 7.0 ppm correspond to aromatic protons, most likely originating from the diisocyanate component (possibly toluene-2,4-diisocyanate), while signals in the range of δ = 3.4 – 1.5 ppm stem from aliphatic -$CH_2$ groups of the diol component (higher chemical shift corresponds to $CH_2$ in α-position to oxygen of the urethane group). Comparing the spectra before and after the hydrogen incubation, no significant changes can be detected.

Figure 3.32 shows $^{13}C$ spectra recorded for the same samples. Again, signals can be assigned corresponding to the diisocyanate and diol components. A chemical shift of δ = 154 ppm originates from the carbonyl groups of the diisocyanate, δ = 137 – 119 ppm originates from aromatic carbon atoms. Signals between δ = 75 – 20 ppm stem from aliphatic carbon atoms, mostly from the diol component. Again, higher chemical shift corresponds to carbon in proximity to oxygen atoms of the urethane group. As already seen for the 1H spectra, no significant changes before and after hydrogen incubation were detected in the material. Thus, it can be concluded that no changes related to the general chemical structure occurred during the treatment as most of the structure is composed of hydrogen and carbon.

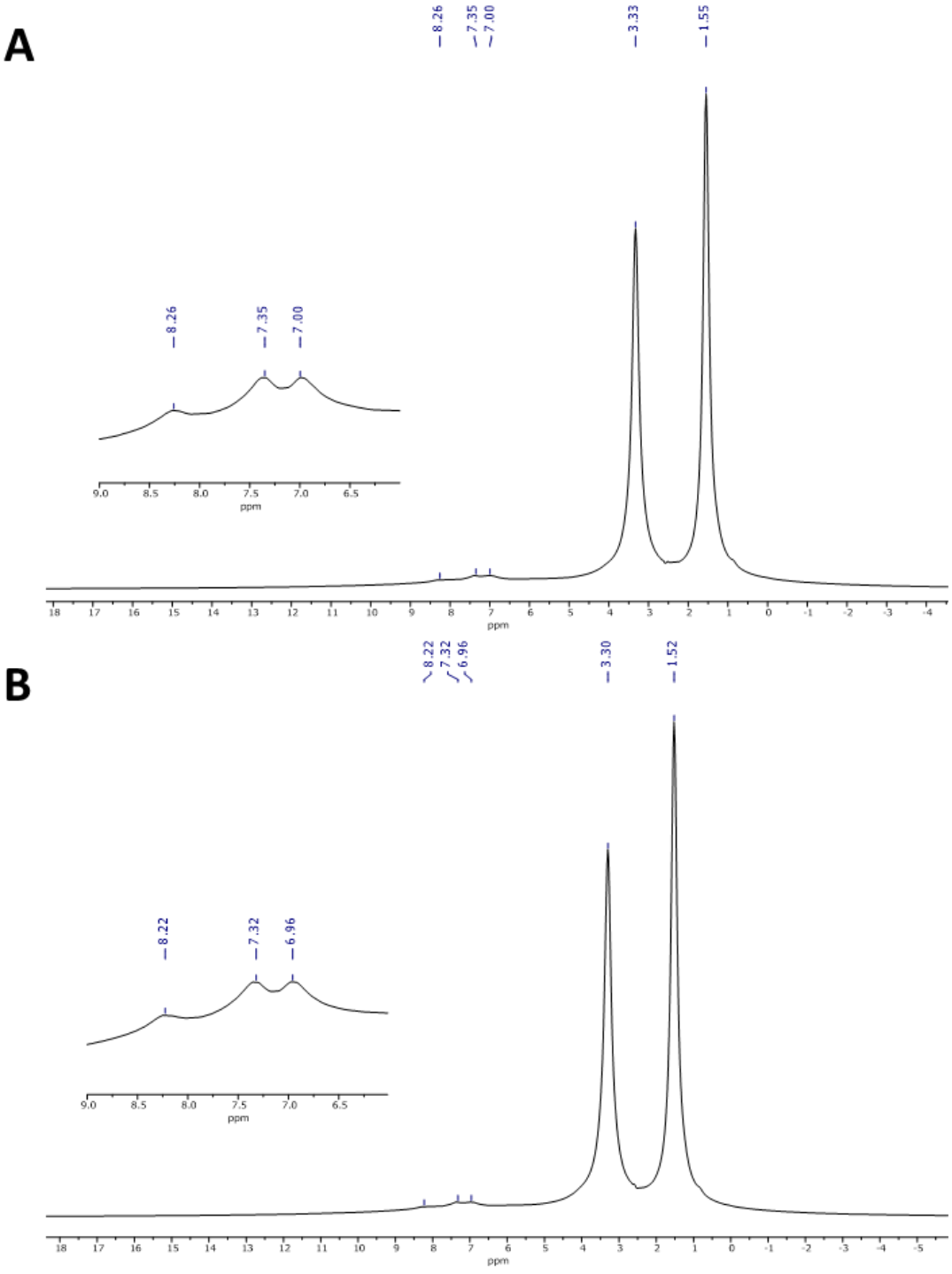


**Figure 3.31.** $^{1}$H NMR spectra of FAT_003 (PU) before (A) and after hydrogen incubation (B) recorded at 300 MHz. The inset shows an enlarged view of the range of δ = 9 – 5 ppm.

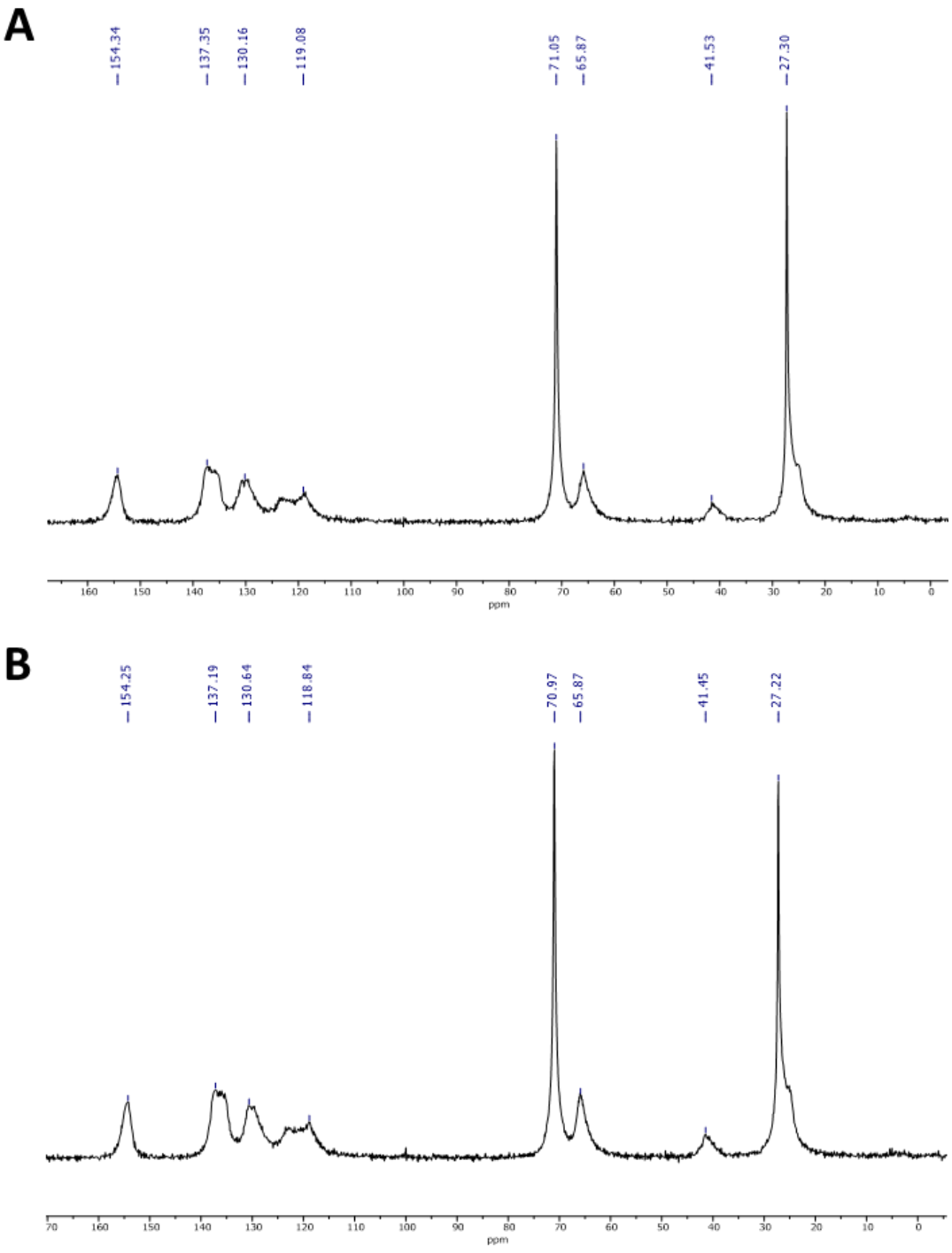


**Figure 3.32.** $^{13}C$ NMR spectra of FAT_003 (PU) before (A) and after hydrogen incubation (B) recorded at 300 MHz.

Next, the same analysis was performed for FAT_004 (PU), which was presumed to have very similar chemical characteristics. As seen in figure 3.33, very similar signals were obtained for the $^{1}H$ NMR spectra before and after hydrogen incubation and they can be assigned to the same structural elements as described above. Again, no significant differences were detected with respect to hydrogen treatment. Similarly, in figure 3.34 the $^{13}C$ NMR spectra of FAT_004 are shown. Also these show signals that can be assigned to the structural elements (diisocyanate and diol components) as described above. Again, no changes before and after hydrogen treatment were visible.

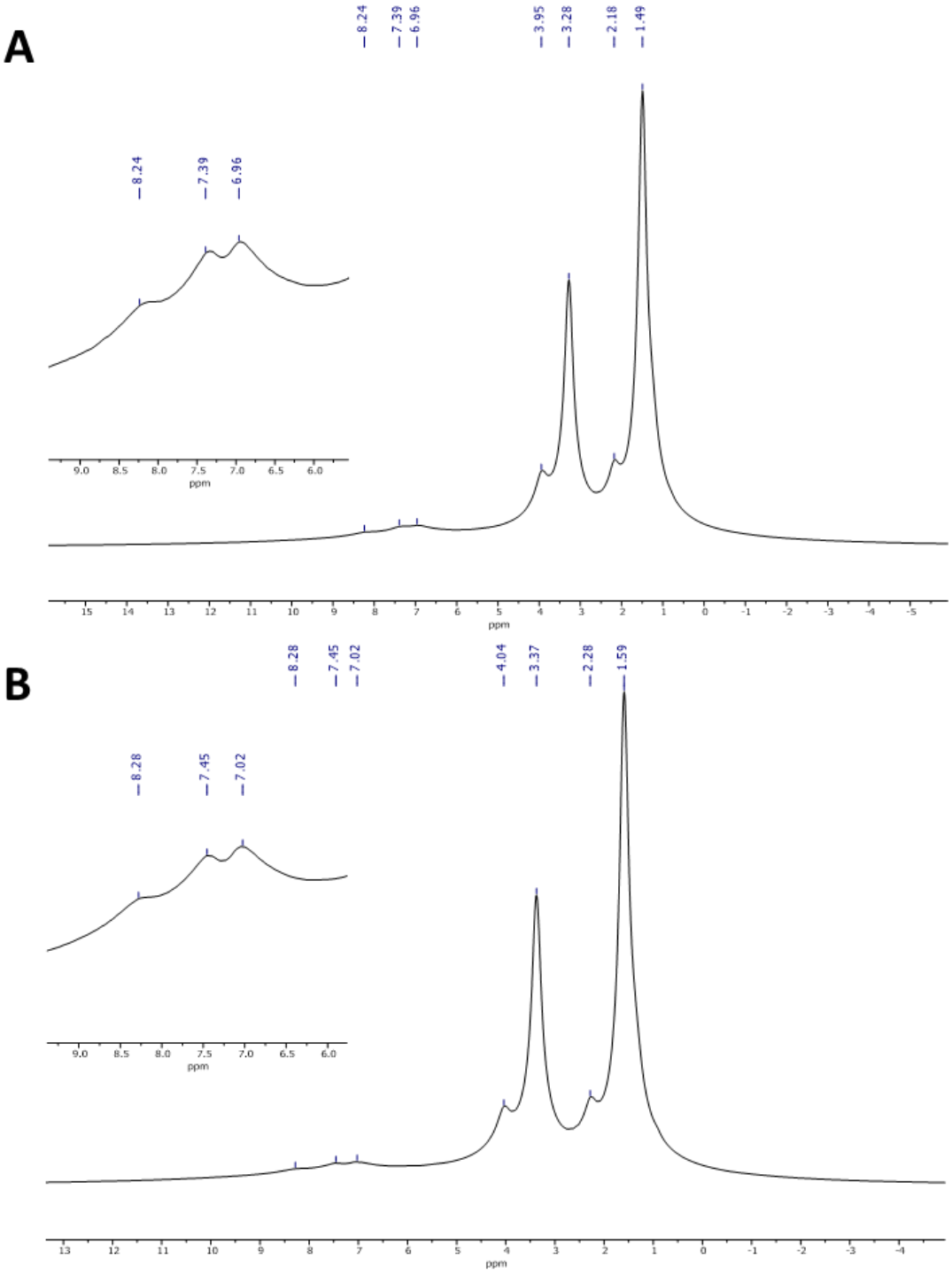


**Figure 3.33.** $^{1}$H NMR spectra of FAT_004 (PU) before (A) and after hydrogen incubation (B) recorded at 300 MHz. The inset shows an enlarged view of the range of δ = 9.5 – 5.5 ppm.

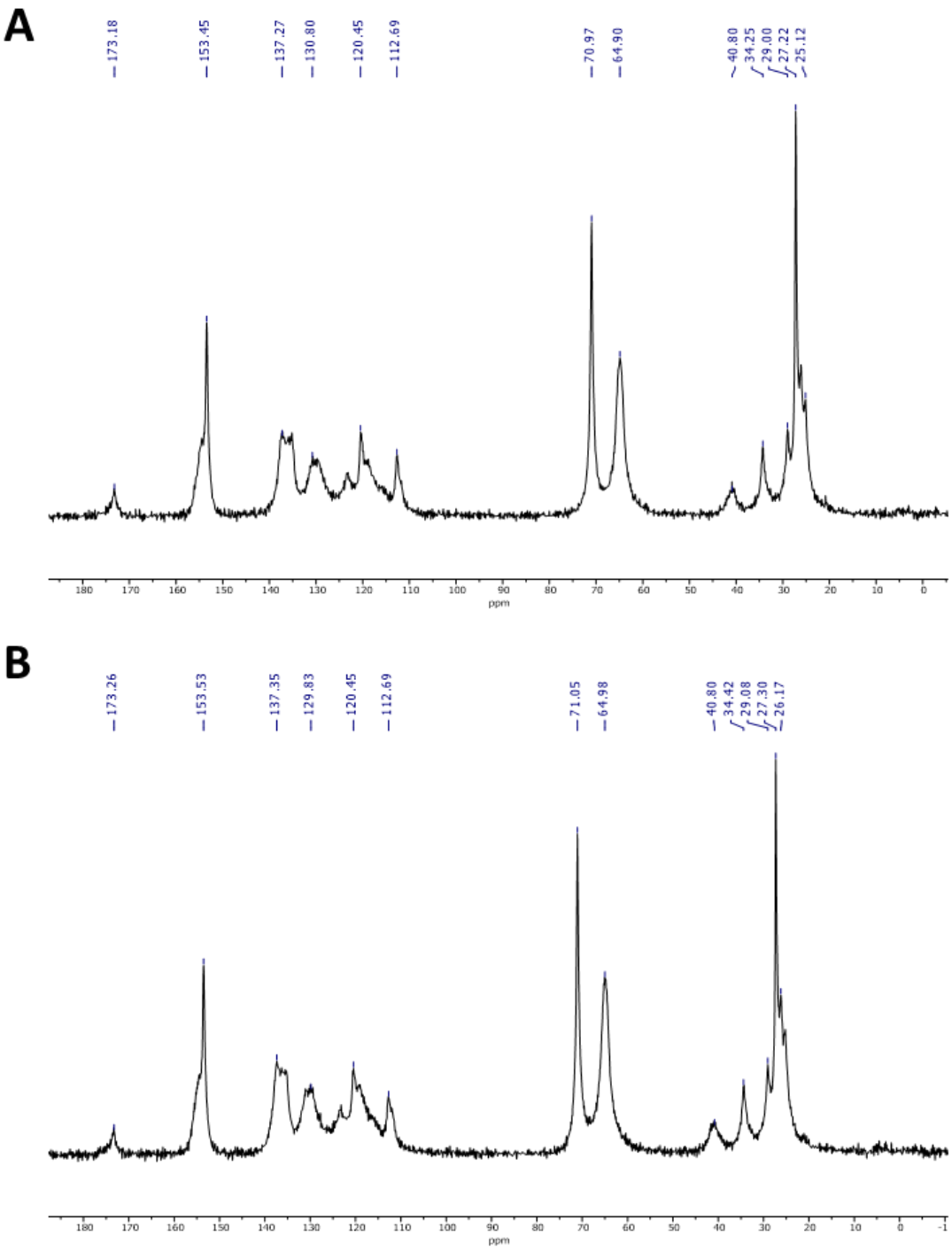


**Figure 3.34.** $^{13}C$ NMR spectra of FAT_004 (PU) before (A) and after hydrogen incubation (B) recorded at 300 MHz.

Finally, $^{1}H$ and $^{13}C$ NMR spectra were recorded for FAT005. After hydrogen incubation, measurements were performed for both FKM batches. As expected only one main signal was detected at a chemical shift of δ = 2.67 ppm both before and after the hydrogen treatment. This signal can be attributed to -$CH_2$ groups stemming from vinyliden fluoride (VDF) used as a monomer. Other typical monomers used for the synthesis of FKM materials do not possess hydrogen in their structure. In figure 3.35 A) and B) slight tailing of the peak towards lower chemical shifts is visible. In figure 3.35 C), a more pronounced signal at δ = 0.04 ppm was detected. These signals probably originate from small fractions of silicone grease or similar compounds present in the FKM material. Obviously, this fraction varies between the two different O-ring batches shown in B) and C). As already seen for the other material samples, also in this case no influence of hydrogen treatment was visible.

Last, $^{13}C$ NMR spectra were recorded for the FKM samples shown in figure 3.36. In this case, again one main signal was observed at δ = 35 ppm, which as well can be attributed to carbon atoms from -$CH_2$- groups.[15, 16] In figure 3.36 C), another very weak signal can be seen at around 150 ppm. This signal might also be present in the other spectra, but covered by the baseline noise. Structurally, it might originate from carbon bound to fluoride (-$CF_2$- or -$CF_3$). Overall, also in this case, no evidence for structural changes due to hydrogen incubation were found. However, to completely assess the chemical composition for FKM, $^{19}F$ NMR spectroscopy measurements would be recommended as reported in literature.[17] In this study, no effects of high pressure hydrogen on the chemical nature of FKM were found, which is good agreement with the here described findings.

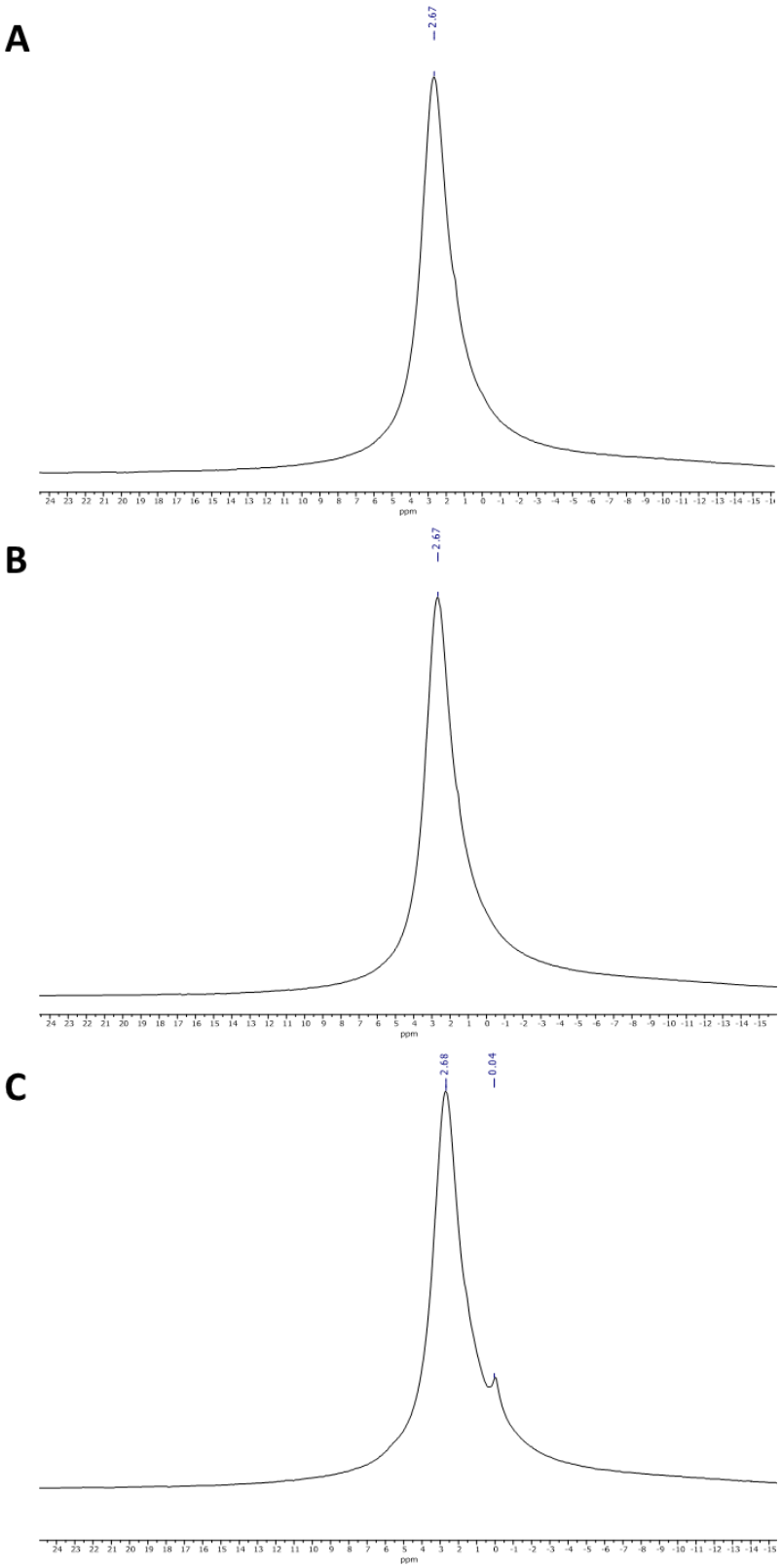


**Figure 3.35.** $^{1}H$ NMR spectra of FAT_005 (FKM) before (A) and after hydrogen incubation, batch 1 (B) and batch 2 (C) recorded at 300 MHz.

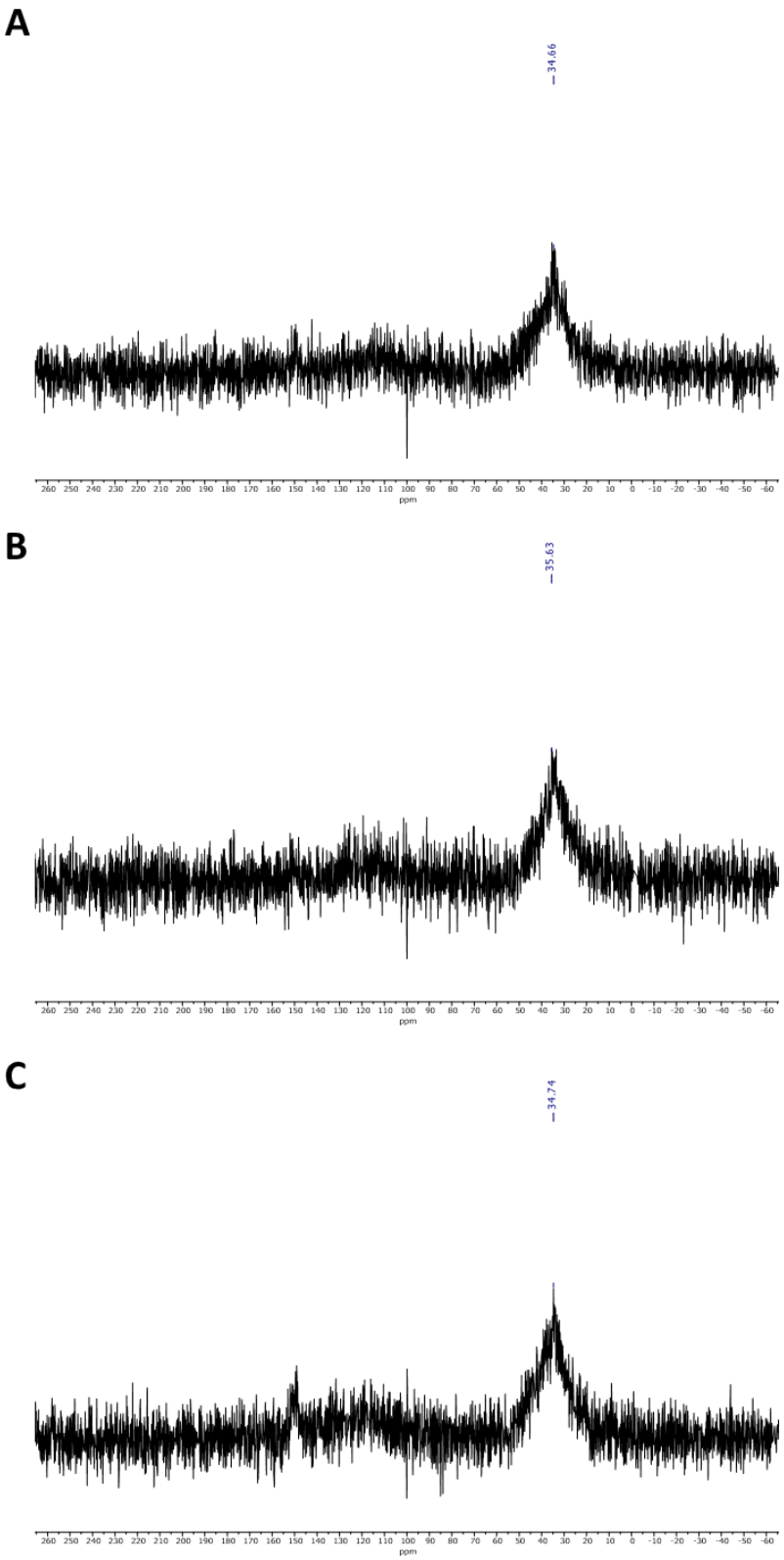


**Figure 3.36.** $^{13}C$ NMR spectra of FAT_005 (FKM) before (A) and after hydrogen incubation, batch 1 (B) and batch 2 (C) recorded at 300 MHz.

## 3.6 $H_2$ adsorption

Finally, for all samples the general hydrogen adsorption capacity was determined via BET (Brunauer –Emmet-Teller) measurements. These measurements were performed on the samples without any pre-treatment. For each sample, a defined mass was placed in the measurement cell. Then, vacuum was drawn on the measurement cell and subsequently the pressure of hydrogen was slowly increased. The amount of adsorbed hydrogen per sample mass was monitored depending on the relative hydrogen pressure (see figure 3.30). For each sample, the final amount of adsorbed hydrogen is summarized in table 3.9 together with the sample surface area calculated according to the BET theory. The calculation is performed under the assumption that only physical interaction between hydrogen and the sample takes place. However, in these measurements it is not possible to distinguish between physisorption and chemisorption. Under the given conditions a chemical reaction between hydrogen and the sample material seems unlikely. The determined amount of adsorbed hydrogen was relatively similar for four out of the five available materials. TPU, PU and FKM samples all adsorbed hydrogen in a range of 0.004 – 0.012 mmol $g^{-1}$ corresponding to surface areas of 0.08 – 0.37 $m^2$ $g^{-1}$, which corresponds to a generally very low hydrogen adsorption. For PEEK, a higher amount of adsorbed hydrogen was recorded (0.124 mmol $g^{-1}$), which also corresponds to a higher available surface area (3.01 $m^2$ $g^{-1}$).

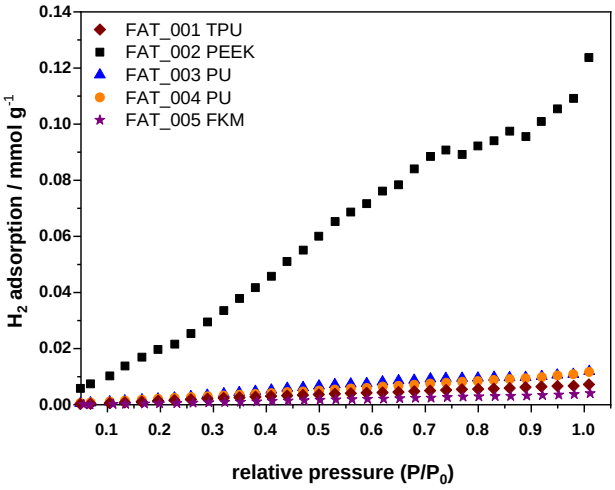


**Figure 3.30.** Hydrogen adsorption determined via BET for all samples without pre-treatment. Measurements were performed at 298 K.[5]

[5] Morsbach et al., Hydrogen Compatibility of Polymers for Fuel Cell Vehicles, Energy Technology 2022, 2200018, DOI: 10.1002/ente.202200018 (CC BY 4.0).

**Table 3.9.** Values for hydrogen adsorption and determined surface area at 298 K and 1 atm.

| sample | $H_2$ (adsorbed) / $cm^3$ $g^{-1}$ | $H_2$ (adsorbed) / mmol $g^{-1}$ | BET surface area/ $m^2$ $g^{-1}$ |
|---|---|---|---|
| FAT_001 TPU | 0.161952 | 0.00723 | 0.1726 |
| FAT_002 PEEK | 2.771328 | 0.12372 | 3.0116 |
| FAT_003 PU | 0.266784 | 0.01191 | 0.3694 |
| FAT_004 PU | 0.261632 | 0.01168 | 0.2231 |
| FAT_005 FKM | 0.090496 | 0.00404 | 0.0847 |

In summary, the amount of hydrogen interacting with a given material surface can be determined via BET measurements. Differences between the materials can be identified, but definite interpretations of the ongoing interaction mechanisms are not possible. It might be that hydrogen diffuses into the materials to a certain extent depending on the material properties (like micro- or nano-porosity). Otherwise, the gas can associate mainly on the sample surface. As the measurement times are rather short and no elevated pressure or temperature conditions are present, these interaction mechanisms seem to be favored. For the analysis of hydrogen compatibility, BET measurements might be helpful to evaluate the sample surface areas available for interaction. The higher the available surface area, the higher is the potential for irreversible hydrogen aging effects. For the determination of hydrogen uptake (physical or chemical) under the chosen storage conditions (335 h, 80 °C, 85 bar), BET measurements are not suitable.

# 4. Experimental Section

## 4.1 Sample treatment (storage conditions)

After receipt of the samples, they were stored in the dark at a constant temperature of T = 20 °C for the duration of the project.

## 4.2 Materials

Tetrahydrofuran (HiPerSolv CHROMANORM) was purchased from VWR International. *N*,*N*-Dimethylformamide (99.9%) was obtained from AppliChem GmbH. Dichloroacetic acid (>99%) was purchased from Acros Organics. Lithium bromide (LiBr, 99%) was procured from Merck KGaA.

## 4.3 SEM

Polymer samples were cut into 1 x 1 cm pieces (shouldered test bars) or 1 cm long O-ring cut-outs. For each sample, the native surface as well as a freeze fracture surface was investigated. To produce fracture planes, 1 cm sample pieces were scratched on the surface, mounted to two holders and subsequently immersed into liquid nitrogen. After the cooling-down of the sample was completed (no bubbling observed anymore), the sample was cracked manually with a second holder along the scratch-line. As an exception, PEEK samples were taken out of the nitrogen and cracked afterwards to achieve better handling possibilities (samples required more force to be cracked).

Morphological characterization of the polymer samples was then performed via Low Voltage Scanning Electron Microscopy (LV-SEM). Imaging was performed on a Leo 1530 Gemini Schottky FEG-SEM microscope with 0.1-1.0 kV landing voltage (exact value is given for each specific micrograph). The application of modern field emission scanning electron microscopes (FE-SEM) allows imaging the native sample surface without sputter-coating.

FKM samples were additionally characterized via EDX (energy dispersive x-ray) spectroscopy measurements on a Hitachi SU8000 FEG-SEM equipped with a Bruker XFlash 5010 Silicon Drift Detector. EDX spectra were recorded and analysed using the ESPRIT 2.1 software.

## 4.4 GPC

For relative molecular weight determinations, PSS SECcurity Agilent 1260 Infinity setups (Polymer Standards Service GmbH (PSS)) were used, including a PSS SECcurity UV detector (254 nm) and a Shodex RI detector.

TPU (FAT_001) and PU samples (FAT_003, FAT_004) were dissolved in THF at a concentration of 1 g $L^{-1}$ and filtered through 0.45 µm Millex-FH filters (Merck, Germany) before injection. Both PU samples were not completely soluble in THF, so that only the solution supernatant containing the soluble fraction was used for analysis. The samples were analysed on a setup containing a column combination from PSS (SDV $10^6$, $10^4$, 500 Å, 300x8 mm) maintained at 30 °C with THF as eluent and a flow rate of 1 mL $min^{-1}$. For evaluation, either the UV (PU - FAT_003, FAT_004) or the RI detector signal (TPU - FAT_001) was used and the molecular weights were determined relative to linear polystyrene (PS) standards provided by Polymer Standards Service (PSS).

PEEK (FAT_002) was subjected to solubility experiments according to a protocol from Agilent Technologies.[1] The obtained sample (FAT_002) was heated in dichloroacetic acid for several days. However, no solubility could be achieved.

FKM (FAT_005) was as well subjected to solubility experiments according to literature.[2] The obtained sample was heated in DMF with 1 mg $mL^{-1}$ LiBr, but again no solubility could be achieved.

## 4.5 DSC

Samples were transferred into DSC sample aluminum pans (100 µL volume, Mettler-Toledo GmbH, Gießen, Germany) and covered with aluminum lids. DSC measurements were performed on a DSC 823 instrument (Mettler-Toledo GmbH, Gießen, Germany). Heating-cooling-heating cycles were recorded with a heating/cooling rate of 10 K $min^{-1}$ between -140 and +520 °C for PEEK (FAT_002) and -140 and +280 °C for all other samples. The measurements were performed under nitrogen atmosphere with a flow of 30 mL $min^{-1}$. For all samples, the second heating cycle was evaluated to avoid effects due to sample history.

## 4.6 TGA

Samples were transferred into aluminum oxide sample pans (ME-24124, 150 µL volume, Mettler-Toledo GmbH, Gießen, Germany). TGA measurements were performed on a TGA/DSC 3 instrument (Mettler-Toledo GmbH, Gießen, Germany). Heating curves were recorded with a heating rate of 10 K $min^{-1}$ between RT and 900 °C for all samples. The measurements were performed for all samples once under nitrogen and once under synthetic air atmosphere with a flow of 50 mL $min^{-1}$ each. For all samples, the mass loss was normalized according to initial sample mass.

## 4.7 Mechanical characterization

**Tensile tests:** Measurements were performed using a materials testing machine Z005 (Zwick/Roell, Germany). Shouldered test bars with thicknesses around 4 mm were drawn with a pre-load of 0.1 N and a rate of 10 mm $min^{-1}$ for TPU (FAT_001) and 1 mm $min^{-1}$ for PEEK (FAT_002) at room temperature. Dependencies of stress vs. draw ratio were recorded in three independent experiments performed at the same conditions.

**Compression tests:** Measurements were performed using a materials testing machine Z005 (Zwick/Roell, Germany). O-ring shape samples (PU - FAT_003) with thicknesses around 4 mm and inner/outer diameter of 2.5 cm/3.3 cm were compressed with a rate of 0.5 mm $min^{-1}$ at room temperature. Dependencies of force vs. compression strain were recorded over five cycles of compression/decompression in three independent compression experiments performed at the same conditions. As the cross-section area of the O-ring shaped samples was not well defined, the stress was not calculated.

## 4.8 Solid-state NMR

For sample preparation, the polymers were shredded with a commercial Waring Laboratory Blender for 5 minutes at highest stage. After filling the measuring rotors, solid state $^{1}H$ and $^{13}C$ CP MAS NMR measurements were carried out using a Bruker Avance II solid state NMR spectrometer operating at 300 MHz Larmor frequency equipped with a standard 4 mm magic angle spinning (MAS) double resonance probe head. Adamantane and L-Alanine were used as reference materials.

### 4.9 BET

The samples were degassed at 120 °C for 6 h under vacuum. The $H_2$ absorption behavior of the samples was measured on a 3Flex Adsorption Analyzer of Micromeritics at 298 K. The saturated pressure was 760 mmHg (1 atmosphere), the pressure change rate was ca. 5 mmHg $min^{-1}$. The data were analyzed using the software MicroActive by Micromeritics. The BET surface area and $H_2$ uptake were calculated via non-local density functional theory (NLDFT) models.

## 5. Conclusion

In this project, five different sample types were selected, subjected to hydrogen aging treatment and subsequently characterized with different analytical methods. For the aging treatment, an elevated temperature of 80 °C was chosen after thermogravimetric analysis, which revealed that all samples were stable under these conditions. Subsequently, various analytical techniques were applied, showing that for all samples differences before and after hydrogen incubation could be detected. This indicates that the chosen treatment conditions (80 °C, 85 bar, 335 h) were suitable to simulate aging processes of the selected materials. In table 5.1, an overview about the performed measurements is shown. Additionally, it is reported whether differences before and after hydrogen treatment were found.

**Table 5.1.** Overview about performed measurements and results concerning detected differences before and after hydrogen aging treatment.

| Sample | Electron microscopy | GPC | TGA | DSC | Mechanical character-ization | ssNMR | BET |
|---|---|---|---|---|---|---|---|
| FAT001 (TPU) | ✓ | X | ✓ | ✓ | X | N.D. | comparison of short-term $H_2$ adsorption capability |
| FAT002 (PEEK) | X | X | ✓ | X | X | N.D. | |
| FAT003 (PU) | ✓ | ✓ | ✓ | X | X | X | |
| FAT004 (PU) | ✓ | X | ✓ | ✓ | N.D. | X | |
| FAT005 (FKM, batch 1) | X | X | ✓ | ✓ | N.D. | X | |

Differences visible: **X** = no, ✓ = yes, N.D. = not determined

In summary, mainly the application of two techniques was very useful to detect changes occurring after hydrogen aging treatment: With electron microscopy, a visual inspection of the material morphology is possible and gives very fast information about the material condition. For fundamental research regarding the individual materials, the high resolution available via electron microscopy is ideal, but for fast screening of a high sample number the resource demand is very high (high equipment cost, personnel effort). Other microscopy methods might be an alternative, but it has to be clarified whether the accessible resolution is suitable to resolve the aging effects. The second method by which it was possible to detect material changes was thermogravimetric analysis. With this technique, aging effects were found for every material sample, which means it is relatively sensitive with respect to the occurring processes. The instrument cost is moderate and also required time and personnel resources are acceptable for sample screening.

In contrast to TGA, only very little effects were visible with differential scanning calorimetry (DSC). The observed effects (differences in heat capacity change) are difficult to interpret and require further knowledge about the materials and effort to obtain meaningful information. Further material changes were only detected via gel permeation chromatography (GPC) but with limited information about the actual processes. Only one material (TPU) showed complete solubility in the available solvents, so that a full characterization via GPC was not possible. Therefore, GPC is not recommended as a routine characterization technique in this study.

Via mechanical characterization and solid state NMR, no aging effects could be found for the chosen materials. This might be due to the fact that not all samples were analysed. Nevertheless, mechanical analysis poses a valuable technique to assess the final material performance (e.g. sealing ability) when it comes to the application. As a significant number of sample specimen is required to obtain reliable statistics, this method might be applied at a later stage, but its inclusion is strongly recommended regarding material safety evaluation. On another note, solid state NMR is able to resolve very detailed chemical information of the sample materials. However, the resource demand is very high (high instrument cost, personnel and time effort) and it is not a routine technique. In this study, no chemical aging effects were found, which is in agreement with the expectations as presumably no double bonds available for hydration are present in the materials. Thus, the application of ssNMR for evaluation of aging effects is not recommended.

Finally, BET measurements were applied to measure the hydrogen adsorption of the materials. Here,



information was obtained for all materials, but it is not possible to distinguish between chemisorption and physisorption. Also, the measurement timescale is much shorter than in the aging conditions and temperature as well as pressure are different. Thus, it is not clear whether the information obtained can be related to real material applications.

The evaluation of all applied techniques is summarized in table 5.2.

**Table 5.2.** Evaluation of characterization techniques regarding their recommendation for the analysis of hydrogen aging effects. Scale ranges from +++ (highly recommended) to 0 (not recommended).

| technique | recommendation | remarks |
|---|---|---|
| (Electron) microscopy | ++ | High resource demand (cost, personnel), very high resolution |
| GPC | 0 | Poor solubility of many materials, little information obtained |
| TGA | +++ | Highest detection rate of aging effects, relatively low resource demand |
| DSC | + | Relatively low resource demand, requires more research effort to interpret effects |
| Mechanical characterization | +++ | Relatively low resource demand, very meaningful information regarding material performance/application, high amount of sample material required to obtain statistical relevance |
| ssNMR | 0 | High resource demand (cost, personnel), information only about chemical changes obtained which seem unlikely, easier options are available |
| BET | + | Conditions are not similar to aging treatment, moderate resource demand |

**Open questions and recommendations**

To further obtain insight about the processes occurring upon the material incubation, it needs to be clarified whether the detected effects are indeed a result of the contact to hydrogen. It is also possible that they are caused by the incubation conditions such as the elevated temperature and pressure. Therefore, future investigations should include reference samples that were incubated under the same conditions but in inert atmosphere, e.g. nitrogen. Further, it is advised to perform microscopy measurements on the same sample specimen before and after the treatments. Only then, production based sample defects can be excluded. In case other sample materials that are potentially prone to hydrogenation will be studied, infrared (IR) spectroscopy is recommended as an alternative technique to analyse the chemical structure of polymers.

In summary, the conducted study presents an overview about possible testing procedures and their applicability for the development of standardization guidelines and yields information about effects occurring after accelerated hydrogen aging treatments.

## 6. References


1. Cleaver, G. *Polyether Ether Ketones on Agilent PLgel MIXED-B with Gel Permeation Chromatography*. 2015.
2. Krueger, R.H., David; Wrobel, Dieter, *Reaktive Fluorpolymere, ein Verfahren zur Herstellung, ein Verfahren zur Herstellung von vernetzten, bepfropften oder modifizierten Fluorpolymeren und deren Verwendung*, E.P. Office, Editor. 1996, BAYER AG, Leverkusen (DE): Germany.
3. Herrera, M., G. Matuschek, and A. Kettrup, *Thermal degradation of thermoplastic polyurethane elastomers (TPU) based on MDI.* Polymer Degradation and Stability, 2002. **78**(2): p. 323-331.
4. Kannan, M., et al., *Thermogravimetric analysis and differential scanning calorimetric studies on nanoclay-filled TPU/PP blends.* Journal of Thermal Analysis and Calorimetry, 2013. **112**(3): p. 1231-1244.
5. Barick, A.K. and D.K. Tripathy, *Preparation and characterization of thermoplastic polyurethane/organoclay nanocomposites by melt intercalation technique: Effect of nanoclay on morphology, mechanical, thermal, and rheological properties.* Journal of Applied Polymer Science, 2010. **117**(2): p. 639-654.
6. Saiani, A., et al., *Origin of Multiple Melting Endotherms in a High Hard Block Content Polyurethane. 1. Thermodynamic Investigation.* Macromolecules, 2001. **34**(26): p. 9059-9068.
7. Patel, P., et al., *Mechanism of thermal decomposition of poly(ether ether ketone) (PEEK) from a review of decomposition studies.* Polymer Degradation and Stability, 2010. **95**(5): p. 709-718.
8. Perng, L.H., C.J. Tsai, and Y.C. Ling, *Mechanism and kinetic modelling of PEEK pyrolysis by TG/MS.* Polymer, 1999. **40**(26): p. 7321-7329.
9. Day, M., J.D. Cooney, and D.M. Wiles, *The thermal degradation of poly(aryl—ether—ether—ketone) (PEEK) as monitored by pyrolysis—GC/MS and TG/MS.* Journal of Analytical and Applied Pyrolysis, 1990. **18**(2): p. 163-173.
10. Kuo, M.C., et al., *PEEK composites reinforced by nano-sized SiO2 and Al2O3 particulates.* Materials Chemistry and Physics, 2005. **90**(1): p. 185-195.
11. Singh, A., et al., *Thermal degradation, kinetic and correlation models of poly(vinylidene fluoride–chlorotrifluoroetheylene) copolymers.* Thermochimica Acta, 2012. **548**: p. 88-92.
12. Kader, M.A. and A.K. Bhowmick, *Thermal ageing, degradation and swelling of acrylate rubber, fluororubber and their blends containing polyfunctional acrylates.* Polymer Degradation and Stability, 2003. **79**(2): p. 283-295.
13. Banik, I., et al., *Thermal degradation studies of electron beam cured terpolymeric fluorocarbon rubber.* Polymer Degradation and Stability, 1999. **63**(3): p. 413-421.
14. Lee Jin, H., et al., *Study on the Thermal Degradation Behavior of FKM O-rings.* 엘라스토머 및 콤포지트, 2018. **53**(4): p. 213-219.
15. Katoh, E., K. Ogura, and I. Ando, *An NMR Study of Poly(vinylidene fluoride) Structure by 1H, 13C, and 19F Triple Resonance Method.* Polymer Journal, 1994. **26**(12): p. 1352-1359.
16. Montina, T., P. Wormald, and P. Hazendonk, *13C Solid-State NMR of the Mobile Phase of Poly(vinylidene fluoride).* Macromolecules, 2012. **45**(15): p. 6002-6007.
17. Lee, C.H., et al., *Nuclear magnetic resonance study of o-ring polymer exposed to high-pressure hydrogen.* Journal of Magnetics, 2017. **22**(3): p. 478-482.

## Bisher in der FAT-Schriftenreihe erschienen (ab 2017)

| Nr. | Titel |
|---|---|
| 292 | Innenhochdruckumformen laserstrahlgelöteter Tailored Hybrid Tubes aus Stahl-Aluminium-Mischverbindun für den automobilen Leichtbau, 2017 |
| 293 | Filterung an Stelle von Schirmung für Hochvolt-Komponenten in Elektrofahrzeugen, 2017 |
| 294 | Schwingfestigkeitsbewertung von Nahtenden MSG-geschweißter Feinbleche aus Stahl unter kombinierter Beanspruchung, 2017 |
| 295 | Wechselwirkungen zwischen zyklisch-mechanischen Beanspruchungen und Korrosion: Bewertung der Schädigungsäquivalenz von Kollektiv- und Signalformen unter mechanisch-korrosiven Beanspruchungs-bedingungen, 2017 |
| 296 | Auswirkungen des teil- und hochautomatisierten Fahrens auf die Kapazität der Fernstraßeninfrastruktur, 2017 |
| 297 | Analyse zum Stand und Aufzeigen von Handlungsfeldern beim vernetzten und automatisierten Fahren von Nutzfahrzeugen, 2017 |
| 298 | Bestimmung des Luftwiderstandsbeiwertes von realen Nutzfahrzeugen im Fahrversuch und Vergleich verschiedener Verfahren zur numerischen Simulation, 2017 |
| 299 | Unfallvermeidung durch Reibwertprognosen, 2017 |
| 300 | Thermisches Rollwiderstandsmodell für Nutzfahrzeugreifen zur Prognose fahrprofilspezifischer Energieverbräuche, 2017 |
| 301 | The Contribution of Brake Wear Emissions to Particulate Matter in Ambient Air, 2017 |
| 302 | Design Paradigms for Multi-Layer Time Coherency in ADAS and Automated Driving (MULTIC), 2017 |
| 303 | Experimentelle Untersuchung des Einflusses der Oberflächenbeschaffenheit von Scheiben auf die Kondensatbildung, 2017 |
| 304 | Der Rollwiderstand von Nutzfahrzeugreifen unter realen Umgebungsbedingungen, 2018 |
| 305 | Simulationsgestützte Methodik zum Entwurf intelligenter Energiesteuerung in zukünftigen Kfz-Bordnetzen, 2018 |
| 306 | Einfluss der Kantenbearbeitung auf die Festigkeitseigenschaften von Stahl-Feinblechen unter quasistatisch und schwingender Beanspruchung, 2018 |
| 307 | Fahrerspezifische Aspekte beim hochautomatisierten Fahren, 2018 |
| 308 | Der Rollwiderstand von Nutzfahrzeugreifen unter zeitvarianten Betriebsbedingungen, 2018 |
| 309 | Bewertung der Ermüdungsfestigkeit von Schraubverbindungen mit gefurchtem Gewinde, 2018 |
| 310 | Konzept zur Auslegungsmethodik zur Verhinderung des selbsttätigen Losdrehens bei Bauteilsystemen im Leichtbau, 2018 |
| 311 | Experimentelle und numerische Identifikation der Schraubenkopfverschiebung als Eingangsgröße für eine Bewertung des selbsttätigen Losdrehens von Schraubenverbindungen, 2018 |
| 312 | Analyse der Randbedingungen und Voraussetzungen für einen automatisierten Betrieb von Nutzfahrzeuge im innerbetrieblichen Verkehr, 2018 |
| 313 | Charakterisierung und Modellierung des anisotropen Versagensverhaltens von Aluminiumwerkstoffen für die Crashsimulation, 2018 |

314 Definition einer „Äquivalenten Kontakttemperatur“ als Bezugsgröße zur Bewertung der ergonomischen Qualität von kontaktbasierten Klimatisierungssystemen in Fahrzeugen, 2018

315 Anforderungen und Chancen für Wirtschaftsverkehre in der Stadt mit automatisiert fahrenden E-Fahrzeugen (Fokus Deutschland), 2018

316 MULTIC-Tooling, 2019

317 EPHoS: Evaluation of Programming - Models for Heterogeneous Systems, 2019

318 Air Quality Modelling on the Contribution of Brake Wear Emissions to Particulate Matter Concentrations Using a High-Resolution Brake Use Inventory, 2019

319 Dehnratenabhängiges Verformungs- und Versagensverhalten von dünnen Blechen unter Scherbelastung, 2019

320 Bionischer LAM-Stahlleichtbau für den Automobilbau – BioLAS, 2019

321 Wirkung von Systemen der aktiven, passiven und integralen Sicherheit bei Straßenverkehrsunfällen mit schweren Güterkraftfahrzeugen, 2019

322 Unfallvermeidung durch Reibwertprognosen - Umsetzung und Anwendung, 2019

323 Transitionen bei Level-3-Automation: Einfluss der Verkehrsumgebung auf die Bewältigungsleistung des Fahrers während Realfahrten, 2019

324 Methodische Aspekte und aktuelle inhaltliche Schwerpunkte bei der Konzeption experimenteller Studien zum hochautomatisierten Fahren, 2020

325 Der Einfluss von Wärmeverlusten auf den Rollwiderstand von Reifen, 2020

326 Lebensdauerberechnung hybrider Verbindungen, 2020

327 Entwicklung der Verletzungsschwere bei Verkehrsunfällen in Deutschland im Kontext verschiedener AIS-Revisionen, 2020

328 Entwicklung einer Methodik zur Korrektur von EES-Werten, 2020

329 Untersuchung zu den Einsatzmöglichkeiten der Graphen- und Heuristikbasierten Topologieoptimierung zur Entwicklung von 3D-Rahmenstrukturen in Crashlastfällen, 2020

330 Analyse der Einflussfaktoren auf die Abweichung zwischen CFD und Fahrversuch bei der Bestimmung des Luftwiderstands von Nutzfahrzeugen, 2020

331 Effiziente Charakterisierung und Modellierung des anisotropen Versagensverhaltens von LFT für Crashsimulation, 2020

332 Charakterisierung und Modellierung des Versagensverhaltens von Komponenten aus duktilem Gusseisen für die Crashsimulation, 2020

333 Charakterisierung und Meta-Modellierung von ungleichartigen Punktschweißverbindungen für die Crashsimulation, 2020

334 Simulationsgestützte Analyse und Bewertung der Fehlertoleranz von Kfz-Bordnetzen, 2020

335 Absicherung des autonomen Fahrens gegen EMV-bedingte Fehlfunktion, 2020

336 Auswirkung von instationären Anströmeffekten auf die Fahrzeugaerodynamik, 2020

337 Analyse von neuen Zell-Technologien und deren Auswirkungen auf das Gesamtsystem Batteriepack, 2020

338 Modellierung der Einflüsse von Mikrodefekten auf das Versagensverhalten von Al-Druckguss-komponenten mit stochastischem Aspekt für die Crashsimulation, 2020

339 Stochastisches Bruchverhalten von Glas, 2020

340 Schnelle, breitbandige Datenübertragung zwischen Truck und Trailer als Voraussetzung für das hochautomatisierte Fahren von Lastzügen, 2021

341 Wasserstoffkompatibilität von Aluminium-Legierungen für Brennstoffzellenfahrzeuge, 2021

342 Anforderungen an eine elektrische Lade- und Wasserstoffinfrastruktur für gewerbliche Nutzfahrzeuge mit dem Zeithorizont 2030, 2021

343 Objective assessment of database quality for use in the automotive research and development process, 2021

344 Review of non-exhaust particle emissions from road vehicles, 2021

345 Ganzheitliche Betrachtung von Rollwiderstandsverlusten an einem schweren Sattelzug unter realen Umgebungsbedingungen, 2021

346 Studie zur Abschätzung der Anwendungspotentiale, Risiken und notwendigen Forschungsbedarfe bei der Verwendung von Glashohlkugeln in Kombination mit thermoplastischem Schaumspritzguss, 2021

347 Typgenehmigungsanforderungen an Level-3-Autobahnsysteme - Hintergrundbetrachtungen zu technischen Anforderungen für eine automatisierte Fahrfunktion, 2021

348 Einfluss der Kantenbearbeitung von Aluminiumblechen auf das Restumformvermögen sowie die Festigkeitseigenschaften unter quasistatischer und schwingender Beanspruchung, 2021

349 Verstärkung dünner formgehärteter Bauteile mittels FVK-Verrippungen, 2021

350 HMI Anforderungen für den automatisierten Individualverkehr unter Berücksichtigung von Leistungsmöglichkeiten und -grenzen älterer Nutzer, 2021

351 Compatibility of polymers for fuel cell automobiles, 2021

352 Entwicklung einer gewichtsoptimierten Batteriegehäusestruktur für Volumenfahrzeuge, 2021

353 Charakterisierung und Modellierung des Deformations- und Versagensverhaltens von nicht-faserverstärkten Thermoplasten unter mehrachsiger Crashbelastung, 2021

354 Untersuchung zum thermischen Komfort im Pkw für den Grenzbereich des Luftzugempfindens, 2021

355 Anforderungen an die Güte, Verfügbarkeit und Vorausschau einer Reibwertschätzung aus Funktionssicht, 2021

356 Entwicklung einer standardisierten Prüfanordnung zur Bewertung der Übernahmeleistung beim automatisierten Fahren, 2022

357 Vorstudie zu Verkehrsemissionen - Räumlich und zeitlich aufgelöste Daten durch Schwarmmessungen, 2022

358 Produktivitätssteigerung und Kostensenkung der laser-additiven Fertigung für den Automobilbau, 2022

359 Analyse der Einflussfaktoren auf die Abweichung zwischen CFD und Fahrversuch bei der Bestimmung des Luftwiderstands von Nutzfahrzeugen mit Fokus auf den Ventilationswiderstand von Nfz-Rädern, 2022

360 Werkstoffmodelle und Kennwertermittlung für die industrielle Anwendung der Umform- und Crash-Simulation unter Berücksichtigung der thermischen Behandlungen beim Lackieren im Prozess bei hochfesten Werkstoffen, 2022

361 Compatibility of polymers for fuel cell automobiles, 2022

# Impressum


| | |
|---|---|
| Herausgeber | FAT<br>Forschungsvereinigung Automobiltechnik e.V.<br>Behrenstraße 35<br>10117 Berlin<br>Telefon +49 30 897842-0<br>Fax +49 30 897842-600<br>www.vda-fat.de |
| ISSN | 2192-7863 |

Verband der Automobilindustrie e.V. (VDA)
Behrenstraße 35, 10117 Berlin
www.vda.de
Twitter @VDA_online

Forschungsvereinigung Automobiltechnik e.V. (FAT)
Behrenstraße 35, 10117 Berlin
www.vda.de/fat

VDA | Verband der Automobilindustrie

FAT | Forschungsvereinigung Automobiltechnik